

Experimental Studies of the  
Thermal Diffusivities concerning  
some Industrially Important Systems

Riad Abdul Abas



**KTH Industrial Engineering  
and Management**

Doctoral Thesis in  
Metallurgical Process Science  
Stockholm, Sweden 2006

**ISRN KTH/MSE--05/96—SE+**

**THMETU/AVH**

**ISBN 91-7178-251-6**

**RIAD ABDUL ABAS Experimental Studies of the Thermal Diffusivities concerning some Industrially Important Systems. KTH 2006**



**KTH Industrial Engineering  
and Management**

# **Experimental Studies of the Thermal Diffusivities concerning Some Industrially Important Systems**

**Riad Abdul Abas**

Doctoral Dissertation

**School of Industrial Engineering and Management  
Department of Material Science and Engineering  
Royal Institute of Technology  
SE-100 44 Stockholm  
Sweden**

---

**Akademisk avdelning som med tillstånd av Kungliga Tekniska Högskolan i  
Stockholm, framlägges för offentlig granskning för avläggande av Teknologie  
doktorsexamen, torsdag den 16 mars 2006, kl.10:00 i F3 , Lindstedsvägen 26,  
Kungliga Tekniska Högskolan, Stockholm**

---

***ISRN KTH/MSE--05/96--SE+THMETU/AVH  
ISBN 91-7178-251-6***

*Riad Abdul Abas. Experimental Studies of the Thermal Diffusivities concerning  
Some Industrially Important Systems*

School of Industrial Engineering and Management  
Department of Material Science and Engineering  
Royal Institute of Technology  
SE-100 44 Stockholm  
Sweden

**ISRN KTH/MSE--05/96--SE+THMETU/AVH**  
**ISBN 91-7178-251-6**  
**The Author**





## ABSTRACT

The main objective of this industrially important work was to gain an increasing understanding of the properties of some industrially important materials such as CMSX-4 nickel base super alloy, 90Ti.6Al.4V alloy, 25Cr.6Ni stainless steel, 0.7% carbon steel, AISI 304 stainless steel-alumina composites, mould powder used in continuous casting of steel as well as coke used in blast furnace with special reference to the thermal diffusivities. The measurements were carried out in a wide temperature range covering solid, liquid, glassy and crystalline states.

For CMSX-4 alloy, the thermal conductivities were calculated from the experimental thermal diffusivities. Both the diffusivities and conductivities were found to increase with increasing temperature. Microscopic analysis showed the presence of intermetallic phases  $\gamma'$  such as  $\text{Ni}_3\text{Al}$  below 1253 K. In this region, the mean free path of the electrons and phonons is likely to be limited by scattering against lattice defects. Between 1253 K and solidus temperature, these phases dissolved in the alloy adding to the impurities in the matrix, which, in turn, caused a decrease in the thermal diffusivity. This effect was confirmed by annealing the samples at 1573 K. The thermal diffusivities of the annealed samples measured at 1277, 1403 and 1531 K were found to be lower than the thermal diffusivities of non-annealed samples and the values did not show any noticeable change with time. It could be related to the attainment of equilibrium with the completion of the dissolution of  $\gamma'$  phase during the annealing process. Liquid CMSX-4 does not show any change of thermal diffusivity with temperature. It may be attributed to the decrease of the mean free path being shorter than characteristic distance between two neighbouring atoms.

Same tendency could be observed in the case of 90Ti.6Al.4V alloy. Since the thermal diffusivity increases with increasing temperature below 1225 K and shows slight decrease or constancy at higher temperature. For 25Cr.6Ni stainless steel, the thermal diffusivity is nearly constant up to about 700 K. Beyond that, there is an increase with temperature both during heating as well as cooling cycle. On the other hand, the slope of the curve increases above 950 K, which can be due to the increase of bcc phase in the structure. 0.7% carbon steel shows a decrease in the thermal diffusivity at temperature below Curie point, where the structure contains bcc+ fcc phases. Above this point the thermal diffusivity increases, where the structure contains only fcc phase. The experimental thermal conductivity values of these alloys show good agreement with the calculated values using Mills model.

Thermal diffusivity measurements as a function of temperature of sintered AISI 304 stainless steel-alumina composites having various composition, viz, 0.001, 0.01, 0.1, 1, 2, 3, 5, 7, 8 and 10 wt%  $\text{Al}_2\text{O}_3$  were carried out in the present work. The thermal diffusivity as well as the thermal conductivity were found to increase with temperature for all composite specimens. The thermal diffusivity/conductivity decreases with increasing weight fraction of alumina in the composites. The experimental results are in good agreement with simple rule of mixture, Eucken equation and developed Ohm's law model at weight fraction of alumina below 5 wt%. Beyond this, the thermal diffusivity/ conductivity exhibits a high discrepancy probably due to the agglomeration of alumina particles during cold pressing and sintering.

On the other hand, thermal diffusivities of industrial mould flux having glassy and crystalline states decrease with increasing temperature at lower temperature and are constant at higher temperature except for one glassy sample. The thermal diffusivity is increased with increasing crystallisation degree of mould flux, which is expected from theoretical considerations.

Analogously, the thermal diffusivity measurements of mould flux do not show any significant change with temperature in liquid state. It is likely to be due to the silicate network being largely broken down.

In the case of coke, the sample taken from deeper level of the pilot blast furnace is found to have larger thermal diffusivity. This can be correlated to the average crystallite size along the structural *c*-axis,  $L_c$ , which is indicative of the higher degree of graphitisation. This was also confirmed by XRD measurements of the different coke samples. The degree of graphitisation was found to increase with increasing temperature. Further, XRD and heat capacity measurements of coke samples taken from different levels in the shaft of the pilot blast furnace show that the graphitisation of coke was instantaneous between 973 and 1473 K.

**Keywords:** laser flash, thermal diffusivity, heat conduction, phonon, electron contribution, crystallisation degree, graphitisation.





## ACKNOWLEDGMENT

First I would like to thank my advisor Prof. Seshadri Seetharaman for his excellence as scientist and scientific adviser. I will never forget how you adopt me as your son, when I was with out any support of anybody. During the difficult time of me, my family and my country, your words were the suitable balm of my suffering.

Special thanks to Professor Mamoun Muhammed for encouragement and the valuable support throughout the work.

I am also grateful to Prof. Miyuki Hayashi for fruitful discussions and inspiring ideas.

Thanks are also due to, Dr. Ragnhild Aune, Dr. Robert Eriksson, Dr. Abdulsalam Uheida and Dr. Anders Jakobsson for their valuable help.

My sons Wasim and Mohammed and my daughter Rokeia. Thank you for all your smiles, which give me a greatest happiness in life.

I would like to thank my family and my friends in Iraq and Sweden for their prayers and encouragement.

I thank all my colleagues working with material science in the department.

A handwritten signature in black ink, appearing to read 'Riad', is written over a horizontal red line.

Riad Harwill Abdul Abas

Stockholm, February 2006

## **Supplements**

**The present thesis is based on the following papers:**

**Suppliment 1: Thermal Diffusivity measurement of CMSX-4 alloy by Laser flash method**

**R. Abdul Abas**, M. Hayashi and S. Seetharaman

Submitted to International Journal of Thermophysics, USA, 2005

**Suppliment 2: Thermal Diffusivity Measurements of some Industrially Important Alloys by a Laser Flash Method**

**R. Abdul Abas**, M. Hayashi and S. Seetharaman

Submitted to Zeitschrift fur Metallkunde, Germany, 2005

**Suppliment 3: Thermal Diffusivity of Sintered Stainless steel-Alumina Composite.**

**R. Abdul Abas** and S. Seetharaman

Accepted for publication in Journal of Metallurgical and Materials Transactions,  
USA, January 2006

**Supplement 4: Effect of Crystallinity on the Thermal Diffusivity of Mould Fluxes for the Continuous Casting of Steels.**

M. Hayashi, **R. Abdul Abas** and S. Seetharaman

ISIJ International, Vol. 44 (2004), No. 4 (April), pp. 691-697.

**Supplement 5: Studies on Graphitisation of Blast Furnace Coke by X-ray Diffraction Analysis and Thermal Diffusivity Measurements**

**R. Abdul Abas**, A. Jakobsson, M. Hayashi and S. Seetharaman

Submitted to Steel Research, Germany, 2005.

The author's contribution to the papers of the thesis:

- I.** Literature survey, experimentation and major part of the writing.
- II.** Literature survey, theoretical analyses, experimentation and major part of the writing.
- III.** Literature survey, experimentation and major part of the writing.
- IV.** Experimentation, result evaluation, participates in the theoretical analysis.
- V.** Experimental work, analysis and evaluation of the experiment results and the major part of the writing.



## TABLE OF CONTENTS

<b>1. INRODUCTION.....</b>	<b>1</b>
<b>1.1 Industrial importance .....</b>	<b>3</b>
<b>2. EXPERIMENTAL .....</b>	<b>5</b>
<b>2.1 Experimental techniques.....</b>	<b>5</b>
2.1.1. Laser flash method .....	5
2.1.2 X-ray diffraction techniques. ....	8
2.1.3. Calorimetric technique.....	9
<b>2.2 Material and samples preparation.....</b>	<b>10</b>
2.2.1. Alloys.....	10
2.2.2. Composites .....	10
2.2.3. Mould powder .....	11
2.2.4. Coke .....	12
<b>3. RESULTS AND DISCUSSION.....</b>	<b>15</b>
<b>3.1 Thermal diffusivity of alloys .....</b>	<b>15</b>
3.1.1. CMSX-4 alloy.....	15
3.1.2. 90Ti.6Al.4V alloy.....	22
3.1.3. 25Cr:6Ni stainless steel .....	25
3.1.4. 0.7% carbon steel .....	28
3.1.5. Electron contribution of thermal conduction of alloys.....	31
<b>3.2 Composites .....</b>	<b>32</b>
<b>3.3 Mould powder.....</b>	<b>40</b>
3.3.1 XRD measurements.....	40
3.3.2 Thermal diffusivity measurements.....	41
<b>3.4 Coke.....</b>	<b>45</b>
3.4.1 XRD measurements.....	45
3.4.2 Heat capacity measurements.....	48
3.4.3 Thermal diffusivity measurements.....	49
<b>3.5. General discussion.....</b>	<b>52</b>
<b>4. CONCOLUSION.....</b>	<b>55</b>
<b>5. FUTURE WORK.....</b>	<b>57</b>
<b>REFERENCES</b>	



## 1. INTRODUCTION

Thermophysical properties such as thermal diffusivity, viscosity and heat capacity are very important from both fundamental as well as practical view points. There are many engineering situations in which the ability of a structural component to either dissipate a large quantity of locally generated heat or conduct heat to/from a material such as ferrous and non-ferrous alloys, metallic matrix composites, mould flux used in continuous casting of steel and blast furnace coke or is of fundamental importance. It is therefore, necessary to determine the thermal transport properties of such materials. If, however improvements in engineering efficiency are to be achieved by improving the heat transfer characteristics, it becomes necessary to understand how, for the material under investigation, heat transport is affected by changes in structure or in the relative proportion of phase's present [1].

In recent years, mathematical modeling of the heat transfer mechanism occurring in high temperature processes has resulted in improvements in process control such as steelmaking and production of heat resistance materials such as Ni-base super alloy and Ti-base alloys. However, reliable values for the thermophysical properties of materials involved are required for the successful operation of these models [2].

The problem of determining the effective thermal conductivity of randomly packed granular materials is one which frequently occurs in engineering practice. A detailed solution of the conduction problem would require knowledge of the shape, size, location and conductivity of each particle in the system together with the interaction between particles. From simplifying hypotheses regarding the dispersion of the discontinuous phase, an overall value of the thermal conductivity can be obtained for a unit cube of the mixture [3].

In the continuous casting of steels, one of the factors affecting the surface quality of the product is the heat transfer process occurring in the mould. It is dominantly influenced by the characteristics of the mould powder infiltrated into the mould/strand gap. The mould powder forms a slag film between mould and solidified steel shell, which frequently consists of glassy, crystalline and liquid layers. Because of the importance of the thermal diffusivity values of slags in heat transfer modeling, they have been measured by different researchers. With respect to the thermal conductivities/ diffusivities of mould flux powder in the glassy and crystalline state, there are very few previous reports available. Shibata et al [4] and Taylor and Mills [5] have reported that the thermal diffusivities of the crystalline samples are higher than those of the glassy samples. However, since the thermal conductivities/ diffusivities of solid slag are considered to be dependent on crystallinity of the samples. Thus, the property should be measured as a function of the degree of crystallisation as well as temperature. Because of the experimental difficulties at high temperature, there are very few accurate data of such properties.



To optimize the blast furnace process, the coke quality and coke consumption rate must be improved. One major factor affecting the coke quality is the degree of graphitisation. It was reported that the higher degree of graphitisation leads to lower reactivities [6, 7]. Earlier studies of the thermal diffusivities of coke samples indicate that, the thermal diffusivity of the coke increases with increase the graphitisation degree of the coke [8, 9]. It is critical to the optimum performance of the furnace to focus on the factors, which could affect the degree of graphitisation. These factors can be temperature, chemical composition and thermal history of the coke.

The methods for measuring the thermal diffusivity can be classified into two main groups: viz. periodic and nonperiodic heat flow methods. The periodic method includes Ångström, thermoelectric and radial wave methods, while the nonperiodic method includes bar, small area, semi-infinite plate, radial heat flow high-intensity arc, electrically-heated rod and flash method [10]. Most of these methods have inherent limitations primarily due to heat transport via convection as well as heat losses by radiation at elevated temperatures. The impact of these factors is minimized by laser flash technique, which is one of the transient methods, due to the small thickness of the sample and the high-speed heat supply to the specimen [11].

The aim of this study is to develop tools for monitoring the progress of a high temperature phenomenon by following the physical property and structural changes by suitable experimental techniques. The scope of the thesis covers precise measurements of

1. thermal diffusivity measurements as a function of temperature of some industrially important alloys, viz, CMSX-4 nickel base super alloy in solid and liquid states, 90Ti.6Al.4V alloy, 25Cr.6Ni stainless steel and 0.7% C steel in solid state.
2. thermal diffusivity as a function of temperature measurements of AISI 304 stainless steel-alumina composites having various compositions.
3. the thermal diffusivities of mould flux in glassy, crystalline and liquid phase,
4. effect of temperature, chemical composition and the thermal history of the coke on the thermal diffusivity and graphitisation degree using thermal diffusivity, X-Ray Diffraction (XRD) and heat capacity measurements .

The first part of the work was conducted as a part of the European Space Agency (ESA) project, THERMOLAB, for precision measurement of thermophysical properties of industrial alloys for optimization of the industrial process design, product quality and resource composition. The third and fourth parts were conducted as part of the projects sponsored by the Swedish Steel Products Association (Jernkontoret) in the research areas T024 and T021 respectively.

## 1.1. Industrial importance

The industrial importance of this work is to use these measurements to get a clear understanding of the phenomena underlying some industrial processes as well as to clarify the impact of structure on properties.

CMSX-4 alloy is designed as a heat resistant and creep resistant alloy for high temperature applications. At high temperatures, the material could be more ductile, but in this alloy, the intermediate particles can be nucleated to be a real obstacle in front of the dislocation slip. On the other hand, these particles increase the structure disorder, which can affect the thermal conductivity. The new generation models for casting of these alloys currently under development contain many more of the actual physical processes involved during solidification, but until now only simplified versions are available. Improved models not only predict solidification rate and temperature profile, but yield valuable information regarding macro- and micro-segregation, freckling and channeling in complex alloys.

In the continuous casting of steel, the mould powder is used to lubricant the mould and to prevent the direct contact between the mould and the product. The heat transfer occurring in the mould is an important factor affecting the surface quality of the product. It is shown that the glassy and liquid states have lower conductivities than the crystalline state. Furthermore, the measurements show that the crystalline state can be controlled by chemical composition of mould powder and the process conditions such as temperature and annealing time.

The present work can be used to optimize the blast furnace process with respect to coke, since the increase of graphitisation degree refers to decrease in the coke reactivity and as a result the coke consumption. It could also be seen that the thermal diffusivity measurements can be a sensitive tool to investigate the graphitisation degree of the coke and the thermal history of the coke sample. Since the present work shows that graphitisation starts at much lower temperatures than that believed earlier, the present results may have an impact on the reduction phenomena occurring in the upper portion of the shaft of the blast furnace.



## 2. EXPERIMENTAL STUDIES

This section will describe relevant details of the materials, experimental techniques and the procedures involved in this work. All the experimental works have been carried out within The Department of Material Science and Technology in KTH.

### 2.1 Experimental techniques

The present work was focused on the measurements of the above-mentioned materials using different techniques, *viz.* laser flash method for thermal diffusivity measurements, X-ray diffraction (XRD) analysis for structural investigations and Differential Scanning Calorimetric (DSC) method for heat capacity measurements. In the following sections, brief descriptions of the techniques are provided.

#### 2.1.1 Laser flash method

A Sinku-Rico laser flash unit (model TC-7000H/MELT), with a maximum sample temperature limit of 1873 K was used for the present thermal diffusivity measurements. A schematic diagram of the same is presented in **Figure 1**. The furnace heating elements, eight in number, are made of lanthanum chromate. The samples were heated under argon atmosphere at the rate of 6 K/min.

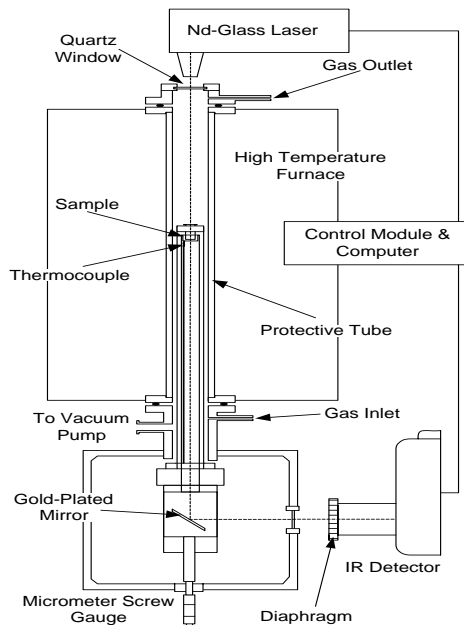


**Figure 1.** Laser-Flash unit schematic diagram.

The sample temperature was measured using a Pt-13%Rh/Pt (R-type) thermocouple positioned in an alumina tube and placed close to the sample holder. In the laser flash technique, the topside of a small disc of material is irradiated with a laser, which provides an instantaneous energy pulse. The laser energy is absorbed on the top surface of a sample and gets converted to heat energy. The thermal energy is conducted through the sample. The temperature rise at the back surface of the sample is monitored using an infrared detector. A plot of the back surface temperature against time is plotted in **Figure 2**. The magnitude of the temperature rise and the amount of laser energy are not required for a thermal diffusivity determination, but only the shape of the curve, which is used in the analysis. The time required for the rear surface to reach half of the maximum temperature rise is denoted as  $t_{1/2}$ . Depending on the specimen and the thermal diffusivity value,  $t_{1/2}$  can range from a few milliseconds to a few seconds. The thermal diffusivity can be expressed as:  $\alpha = 1.37L^2/\pi^2 t_{1/2}$ . Where L is the sample thickness[12].

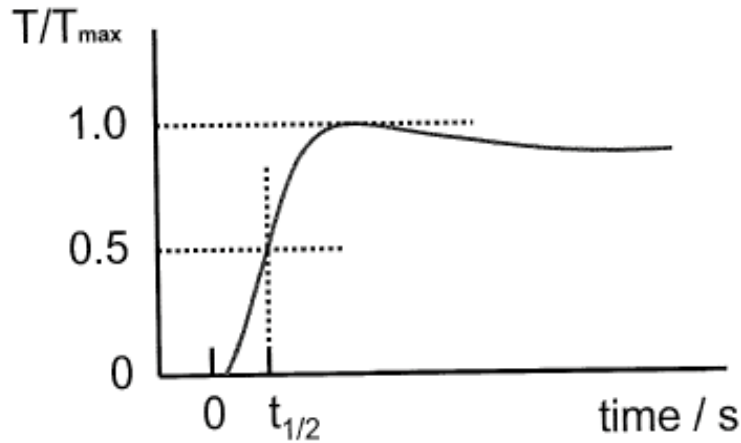


**Figure 2.** The recorded temperature history at the rear surface of a specimen calculated by instrument.

Discs having 10-14 mm in diameter and approximately 2-4 mm in thickness were machined from the solid sample bulks to fit the experimental unit. For CMSX-4 and 90Ti.6Al.4V alloys, a sapphire crucible, which is transparent to laser beam and infrared rays, was used as holder. Titanium foils were placed close to sample as a local oxygen getter in the argon gas atmosphere and, thereby protect the sample from oxidation.

For liquid alloy, the sample is sandwiched between two sapphire crucibles to get an accurate thickness as shown in **Figure 3a**. It can be noted that the crucibles are transparent to the laser beam as well as infrared ray.

In the case of molten mould flux, the three- layered cell arrangement was employed. The three layers are composed of the liquid sample having the form of a thin film, sandwiched between two platinum crucibles. The laser pulse is exposed on the top surface of the upper crucible and the temperature rise on the rear surface of the lower crucible is monitored as a function of time. The experiment is repeated by varying the sample thickness. **Figure 3b** shows the schematic of three- layered arrangement.

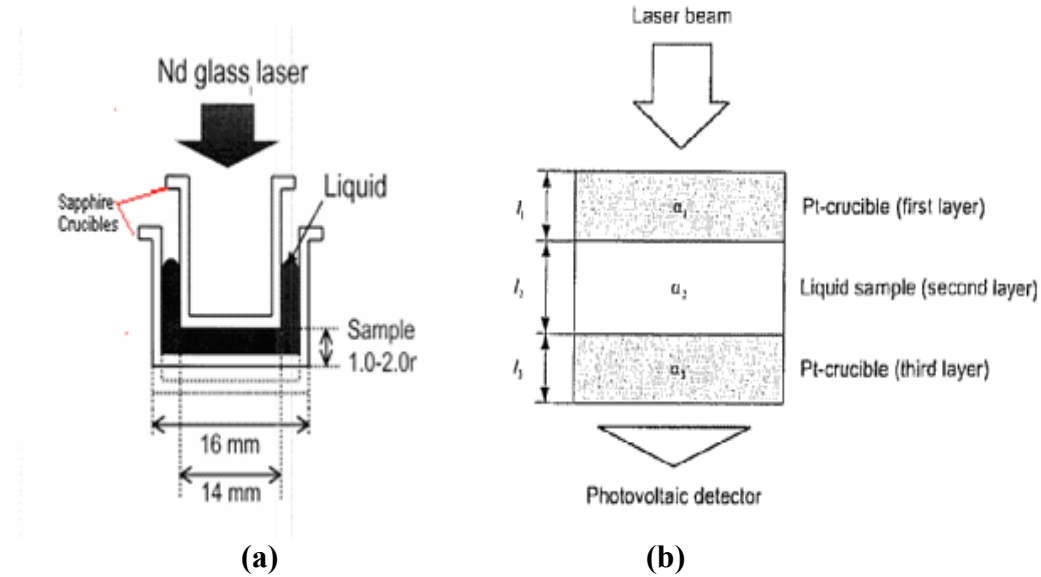


**Figure 3. (a)** Sample arrangement during liquid alloy thermal diffusivity measurement, **(b)** Schematic diagram shown the three-layered cell arrangement in the case of liquid mould fluxes.

The measurements at high temperatures were carried out in an inert atmosphere in order to prevent chemical reactions with the atmosphere. The impurity levels in the commercial argon gas had to be brought down significantly, especially the oxygen potential. In order to lower the impurity levels in the argon gas, it was subjected to a number of purification steps. The gas cleaning system used in the present work is schematically presented in **Figure 4**. The moisture impurity in the argon gas was removed by passing the gas successfully through silica gel as well as  $\text{Mg}(\text{ClO}_4)_2$ . To remove traces of  $\text{CO}_2$  in the gas, a column of ascarite was introduced in the gas-cleaning system. The gas was passed through columns of copper and magnesium turnings kept at 923 K and 723 K respectively [13]. The final partial pressure of oxygen in the argon purified in this way was found by using a  $\text{ZrO}_2\text{-CaO}$  oxygen sensor to be less than  $10^{-13}$  Pa.

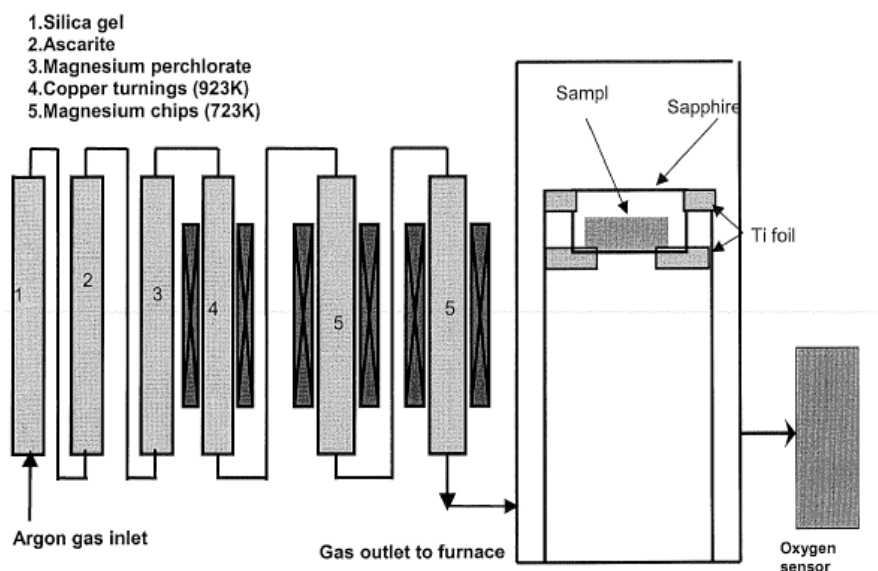


**Figure 4.** The gas cleaning system.

### 2.1.2 X-ray diffraction technique

X-ray diffractometer, Philips X-pert system at the Royal Institute of Technology KTH, Stockholm, Sweden was used in the present work. The sample, either milled coke or mould slag sample, was placed on the platinum strip, which could also be used as a heater. Scattering intensities from copper  $K\alpha$  (wavelength  $\lambda$  is 1.54 Å) were used (50 kV, 40 mA) for the diffraction studies.

For coke study, it was found by preliminary trials that the typical reflection angle  $2\theta$  of the crystalline graphite (002) is  $26^\circ$ , which was most appropriate for monitoring the graphitisation reaction [14]. The samples were scanned over peak (002) in the scanning range  $(20-30)^\circ$  in steps of  $0.02^\circ$ . Isothermal measurements were carried out at 973, 1073, 1173, 1273, 1373 and 1473 K in order to investigate the effect of the time and temperature on the degree of graphitisation.

In the case of mould flux, X-ray diffraction studies were carried out for the glassy and crystalline samples in order to determine the phase and the degree of crystallisation. X-ray diffraction profiles of crystalline samples have shown that the component can be cuspidine ( $\text{Ca}_4\text{Si}_2\text{O}_7\text{F}_2$ ) or nepheline ( $\text{Na}_3\text{KAl}_4\text{O}_{16} - \text{NaAlSiO}_4$ ). Because the largest peak of  $\text{Mn}_2\text{O}_3$  at  $2\theta = 32.951^\circ$  does not overlap with any crystalline peaks of the sample and the largest peak of cuspidine at  $2\theta = 29.150^\circ$  does not overlap with any of the peaks of  $\text{Mn}_2\text{O}_3$ , the degree of crystallisation was defined as the ratio of the largest peak intensity

of the cuspidine to that of  $\text{Mn}_2\text{O}_3$  observed for X-ray diffraction profile of the well-mixed powder of 1g of samples and 0.15 g of  $\text{Mn}_2\text{O}_3$ .

### 2.1.3 Calorimetric technique

An illustration of the NETZCH STA 449C Jupiter unit used in the present work is presented in **Figure 5**. The apparatus was calibrated against In, Sn, Zn, Ag and Au. Fusion temperature and heats of fusion were in agreement with the literature [15]. The DSC measurements were initiated by placing the CMSX-4 alloy into a platinum crucible closed with a platinum lid [16] or milled sample of the coke into an alumina crucible closed with an alumina lid and positioned, along with a reference with similar size specifications, on the platinum sample holder provided with a previously calibrated type S (Pt-10%Rh/Pt) thermocouple. Both crucibles were weighed before and after each DSC measurement and placed in exactly the same position throughout the measurement series. Before the experiment was started, the furnace chamber was repeatedly evacuated and flushed with purified 99.99999% Ar three times.

The DSC measurement was conducted in the temperature range of 300- 1573 K with a rate of 10 K/min in heating and cooling cycles. An initiating stabilising level at 313 K was used before the commencement of the temperature program. For a standard reference, sapphire was employed.

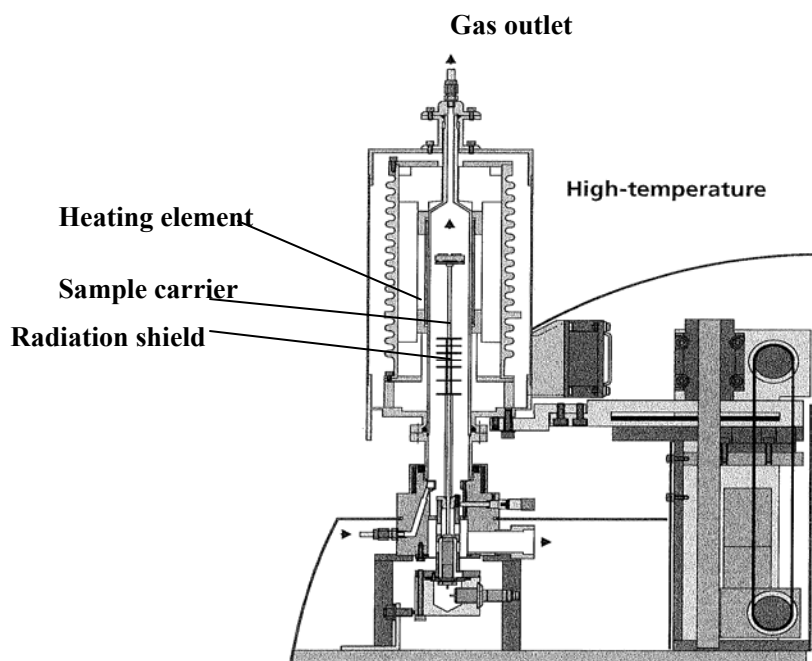


**Figure 5.** Schematic of NETZCH STA 449C Jupiter unit used in the present work [15].



## 2.2. Materials and samples preparation

### 2.2.1. Alloys

CMSX-4 nickel base super alloy and 90Ti.6Al.4V alloy used in present work were supplied by Doncasters Precision Castings, Bochum GmbH, Germany. 25Cr.6Ni stainless steel was supplied by AB Sandvik Steel, Sweden and 0.7% carbon steel was supplied by CORUS Steel, The Netherlands. The chemical compositions of the alloys are presented in **Table I** [17].

**Table I.** Chemical compositions in mass % (except for O and S which are in ppm) of the alloys used in present work [17].

Alloy	Composition
CMSX-4	Ni 60.5, Al 5.6, C 0.004, Cr 6.4, Fe 0.04, Mo 0.61, Re 2.9, Si 0.4, Ti 1.05, Ta 6.5, W 6.4, O 2*, S 2*
Ti alloy	Ti 90, Al 6, V 4
Stainless steel	Fe, 62.82, C 0.014, Si 0.38, Mn 0.48, Cr 25.61, Ni 6.49 Mo 3.95, N 0.252
Steel	Fe 97.81, C 0.71, Si 0.35, Mn 1.09, P 0.011, S 0.02, N 0.0044, O 0.0008

\* indicates ppm

### 2.2.2 Composite material

The composite samples used in the present work are prepared using powder sample of stainless steel AISI 304 ( Cr 17-20%, Mn < 2%, Ni 8-11%, C < 0.08%, Fe balance) with particle size less than 40  $\mu\text{m}$  and aluminum oxide powder with particle size less than 10  $\mu\text{m}$ . Well-mixed composite stainless steel- alumina samples with (0.001, 0.01, 0.1, 1, 2, 3, 5, 7, 8 and 10 wt %)  $\text{Al}_2\text{O}_3$  were pressed into pellets using piston-cylinder die and hydraulic press of 12 mm in diameter.

The amount of the mixture used was 3 g and the compaction pressure was about 1900 Mpa. The pressed samples were sintered at 1673 K for 20 hours using vertical furnace equipped with super Kanthel heating elements. The densities of the samples were

calculated using weight and volume and were found to be 98.5-99% of the theoretical density of the same composition.

### 2.2.3 Mould powder

The chemical compositions of the four proprietary mould powders used in Swedish steel industry are given in **Table II**. The mould powders were decarburised by heating in air for 48 h at 1073 K. The decarburised powders were placed in platinum crucibles and melted in air for 0.25 h at 1623 K for powder A, and at 1573 K for powders B-D. Glassy samples were prepared by pouring the melts onto a stainless steel plate kept at 773 K. Subsequently, the samples were annealed in air for 1h at 773 K and cooled down at the furnace-cooling rate to eliminate the residual stresses. Discs having about 12 mm in diameter and 1.5 to 2.5 mm in thickness were machined from the glassy samples. Annealing of the glassy samples having the disc shape at 1073 and 1173 K for 1-120 h led to their crystalline structure. Since the surfaces of the annealed samples became very rough because of the crystallisation, the surfaces were polished to obtain the parallelism between both faces.

**Table II.** Chemical compositions of the proprietary mould powders (mass%).

	A	B	C	D
SiO <sub>2</sub>	25.5	32.7	34.2	28.8
CaO	22.7	28.8	29.4	36.5
MgO	0.97	1.77	1.01	1.3
Al <sub>2</sub> O <sub>3</sub>	12	4.7	3.92	6.5
TiO <sub>2</sub>	0.46	0.11	0.1	0.3
Fe <sub>2</sub> O <sub>3</sub>	2.86	1.24	1.09	0.8
MnO	0.04	< 0.10	0.05	3.3
Na <sub>2</sub> O	2.62	11.3	12.8	7.2
K <sub>2</sub> O	1.43	0.31	0.37	0.1
F	4.42	9.4	7.95	5.9

#### 2.2.4 Coke

The sampling scheme of coke taken out from the Experimental Blast Furnace EBF at MEFOS Luleå, Sweden is schematically depicted in **Figure 6**. Coke sampling was carried out after nitrogen quenching followed by a carefully documented dissection, where approximately 20-35 pieces were taken out at different radial locations and different levels. The samples (approximately 6-8 cm<sup>3</sup>) used in the present investigation are denoted as KL05, KL10, KL15, KL25, and KL35. The distance (mm) of the levels KL05, KL25 and KL35 from the top are about 3961, 6652 and 6981 mm respectively. At each level, coke samples were taken from the centre (C), the place just beside the wall (R) and in between (M).

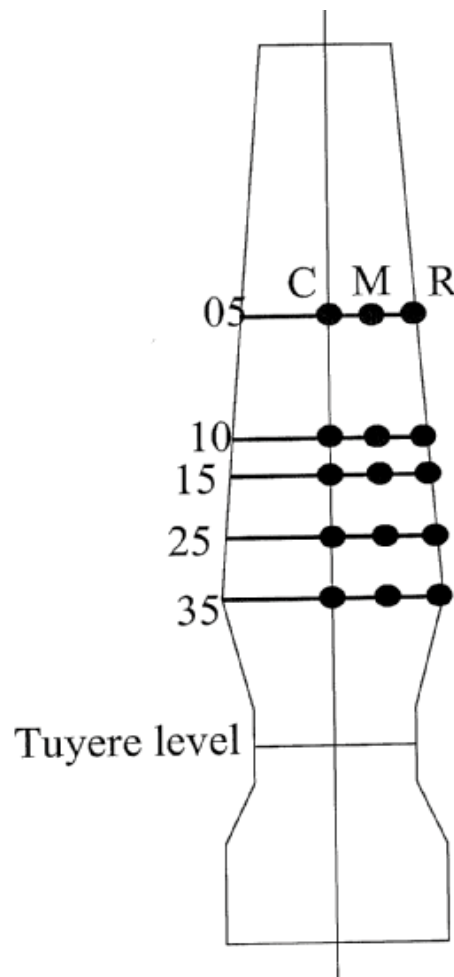


**Figure 6.** Schematic diagram of the experimental blast furnace [6].

A chemical analysis of the samples from the quenched pilot blast furnace is presented in **Table III**. Pellets having 10 mm in diameter and approximately 3 mm in thickness were machined from coke lumps to fit the experimental unit specification.

**Table III.** Chemical analysis in wt% of coke samples from the experimental blast furnace [6].

	Fe [%]	CaO [%]	SiO <sub>2</sub> [%]	P <sub>2</sub> O <sub>5</sub> [%]	S [%]	Al <sub>2</sub> O <sub>3</sub> [%]	MgO [%]	Na <sub>2</sub> O [%]	K <sub>2</sub> O [%]	TiO <sub>2</sub> [%]	C [%]
<b>Feed</b>	0.4	0.08	6.12	0.03	0.58	2.85	0.06	0.13	0.15	0.17	89.43
<b>05C</b>	0.42	0.01	5.76	0.03	0.59	2.63	0.06	0.1	0.17	0.16	90.17
<b>10C</b>	0.46	0.04	6.39	0.03	0.5	2.77	0.06	0.16	0.35	0.17	89.11
<b>15C</b>	0.37	0	6.3	0.024	0.54	2.65	0.06	0.43	1.24	0.15	88.34
<b>20C</b>	0.32	0.02	5.58	0.023	0.51	2.57	0.07	0.61	1.78	0.14	88.48
<b>25C</b>	0.32	0.02	5.83	0.024	0.47	2.61	0.08	0.67	2.31	0.14	87.61
<b>30C</b>	0.34	0.04	5.97	0.025	0.5	2.66	0.08	0.68	2.07	0.14	87.61
<b>35C</b>	0.27	0	5.81	0.22	0.44	2.64	0.08	0.85	3.21	0.12	86.66
<b>05M</b>	0.49	0.07	6.22	0.029	0.54	2.85	0.08	0.14	0.2	0.18	89.25
<b>10M</b>	0.45	0.06	6.17	0.031	0.56	2.7	0.07	0.2	0.35	0.17	89.32
<b>15M</b>	0.4	0.05	6.15	0.031	0.51	2.8	0.22	0.48	1.67	0.14	87.63
<b>20M</b>	0.29	0.03	5.93	0.022	0.47	2.65	0.09	0.83	2.71	0.13	86.94
<b>25M</b>	0.31	0.03	5.41	0.022	0.49	2.43	0.09	0.75	2.43	0.13	88.02
<b>30M</b>	0.33	0.01	5.86	0.022	0.48	2.65	0.07	0.91	2.92	0.12	86.7
<b>35M</b>	0.27	0.04	5.78	0.019	0.43	2.61	0.12	1.22	3.54	0.11	85.95
<b>05R</b>	0.4	0.05	6.34	0.029	0.54	2.95	0.07	0.13	0.25	0.17	89.17
<b>10R</b>	0.96	0	10.64	0.012	0.16	1.73	9.19	0.82	1.91	0.05	74.18
<b>15R</b>	0.25	0.03	5.63	0.023	0.44	2.54	0.1	1.05	3.65	0.11	86.28
<b>20R</b>	0.24	0.03	5.58	0.03	0.54	2.68	0.11	1.17	3.96	0.11	85.71
<b>25R</b>	0.23	0.04	5.95	0.022	0.4	2.61	0.14	1.32	4.7	0.1	84.58
<b>30R</b>	0.22	0	5.65	0.023	0.43	2.54	0.1	0.93	5	0.09	85.13
<b>35R</b>	0.22	0	5.53	0.02	0.42	2.41	0.09	1	4.49	0.1	85.83



### 3. RESULTS AND DISCUSSION

Thermal diffusivity measurements of four different industrially systems, viz, metallic alloys, metallic matrix composites, mould fluxes and coke have been carried out in the present work. The influences of microstructure, phase compositions, temperature and the thermal history of these systems have been studied in present work.

XRD measurements were carried out to investigate the effect of time, temperature and chemical composition on the graphitisation phenomenon of coke using in the blast furnace. Furthermore, XRD analysis was employed in order to determine the crystallisation degree of the mould flux as a function of annealing temperature and time. The effect of crystallisation degree as well as temperature on the thermal diffusivity of mould flux has been carried out.

Heat capacity measurements of coke and CMSX-4 nickel base alloy have been carried out. Furthermore, microstructural investigations of some of these systems using Scanning Electron Microscope (SEM) equipped with Electron Dispersion Spectroscopy (EDS) also were investigated.

The following sections describe the results of the above mentioned measurements and a discussion of the same.

#### 3.1 Thermal diffusivity measurements of alloys

##### 3.1.1 CMSX-4 nickel base alloy

**Figure 7** shows the phase diagram of an alloy close to that of CMSX-4 nickel base alloy used in the present work calculated using Thermo-calc software. For the sake of simplicity, Ti (1.05 wt%) was not taken into account in these calculations. It can be seen that the material contains fcc+bcc+hcp+Ni<sub>3</sub>Al ( $\gamma'$  phase) at the temperature below 1273 K. In the presence of Ti, corresponding Ti-containing phases could be expected. Above this temperature, only fcc+bcc phases are stable and the  $\gamma'$  phase starts dissolving in significant amounts into the metal matrix. According to **Figure 7**, the solidus temperature is 1609 K and liquidus temperature is 1670 K.

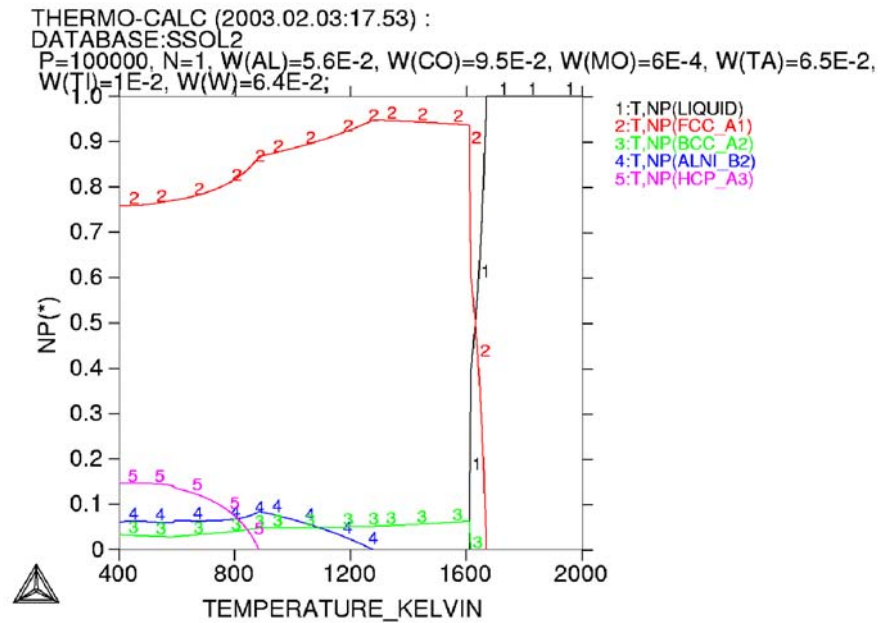


**Figure 7.** Calculated phase diagram of an alloy with composition close to the present CMSX-4 alloy using Thermo-calc software.

In **Figure 8**, all the experimental results of the thermal diffusivity measurements with as received alloy samples are presented as functions of temperature. It can be seen that the thermal diffusivity increases with temperature up to 1223 K. Above this temperature, the diffusivity shows a slight decrease and/or become constant. In the solid-liquid zone, it is difficult to observe any definite trend as the experimental scatter is significant. In fact, above 1223 K, different experimental runs give varying results, which could be due to the thermal history of the industry sample received.

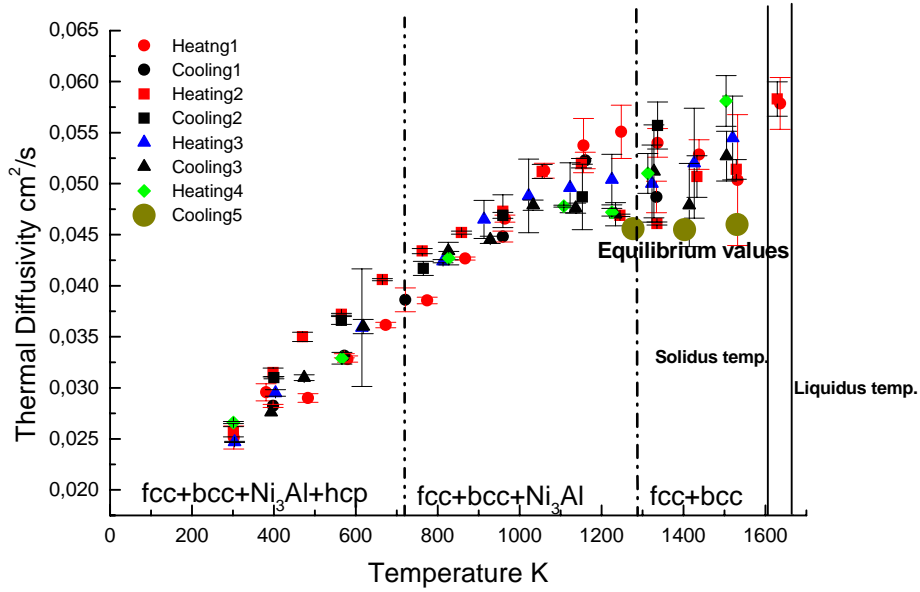


**Figure 8.** Thermal diffusivity-temperature curves of CMSX-4 alloy including the equilibrium values.

**Figure 8** shows also that there is no significant change in the thermal diffusivity values after annealing during isothermal measurements (cooling 5) at 1277, 1403 and 1531 K as a function of time or temperature and that the values obtained after annealing are lower than those measured without annealing treatment. This is indicative of the attainment of thermodynamic equilibrium, where the dissolution of the intermediate phases in the matrix might have been completed and the attainment of impurity levels in the matrix was in maximum.

The thermal conductivities of the CMSX-4 alloy were calculated from experimental thermal diffusivities using the values of the specific heat and density according to the formula

$$\kappa = \alpha \cdot C_p \cdot \rho \quad (1)$$

where “ $\kappa$ ” is the thermal conductivity  $\text{W} \cdot \text{m}^{-1} \cdot \text{K}^{-1}$ , “ $\alpha$ ”, the thermal diffusivity  $\text{m}^2 \cdot \text{s}^{-1}$ , “ $C_p$ ”, the heat capacity  $\text{J} \cdot \text{Kg}^{-1} \cdot \text{K}^{-1}$  and “ $\rho$ ” the density  $\text{Kg} \cdot \text{m}^{-3}$ .

The heat capacity and density values of the alloys investigated in the present work have been reported by [16] and [17] respectively. For the above calculations, the average values of thermal diffusivities from **Figure 8** were used. The thermal conductivities calculated from above formula can be shown in **Figure 9**.



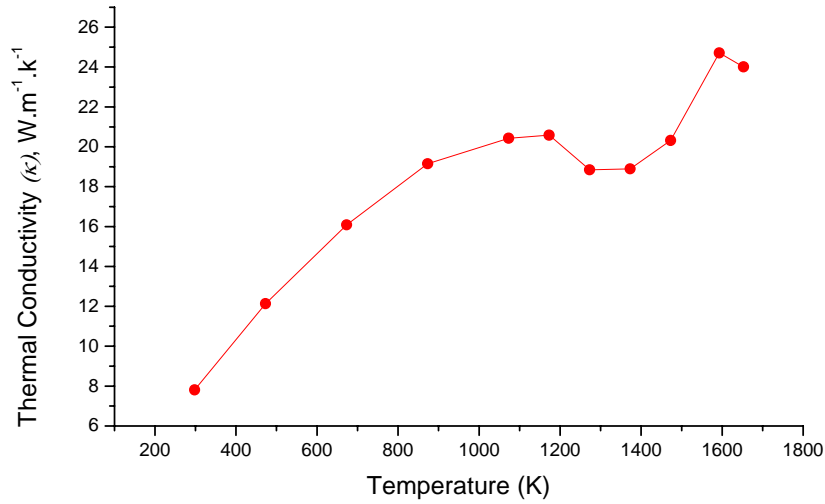


**Figure 9.** The Thermal conductivity of CMSX-4 alloy with respect to temperature.

For structure studies of this alloy, samples A and B were heated to 600 and 1000 K, respectively, at the rate of 6 K/min and subsequently quenched into water. Samples C and D were heated to 1573 K at first, then cooled to 600 and 1000 K, respectively, at the rate of 6 K/min, and then quenched into water in order to determine the effect of microstructure of the alloy on the temperature dependence of the thermal diffusivity. On the other hand, sample E was heat-treated at 1373 K for 30 minutes and quenched in water. **Figure 10** shows the microstructure of the heat treated samples (A-E) as well as received sample. **Table IV** shows the phase composition of these samples using EDS attached to SEM.

The thermal diffusivity measurements of samples A-E, quenched from different temperatures show almost same value. This value is close to the thermal diffusivity of the raw sample at room temperature.

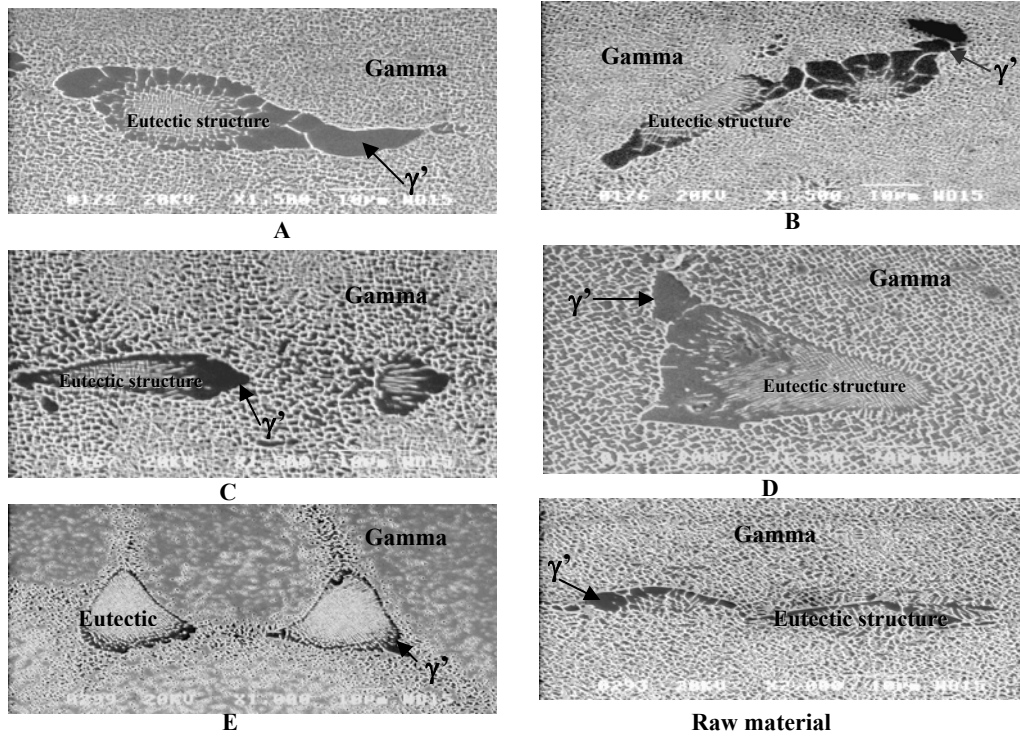


**Figure 10.** SEM pictures of annealed CMSX-4 alloy during: **A,B)** quenched from 600, 1000 K, **C,D)** quenched samples after heating to 1573 and cooling down 600 and 1000 K, **E)** heat treated sample at 1373 K for 30 minutes and quenched in water and raw material.

**Table IV.** Main chemical composition wt% of annealed CMSX-4 samples A-D using EDS attached to SEM.

<b>Spectrum</b>	<b>Ni</b>	<b>Co</b>	<b>Cr</b>	<b>Ti</b>	<b>Si</b>	<b>Al</b>	<b>Re</b>
<b>Raw material</b>							
<b>Matrix <math>\gamma</math></b>	<b>63.02</b>	<b>11.20</b>	<b>8.02</b>	<b>0.96</b>	<b>2.20</b>	<b>4.02</b>	<b>4.81</b>
<b>Eutectic</b>	<b>70.55</b>	<b>9.93</b>	<b>5.30</b>	<b>1.37</b>	<b>3.68</b>	<b>5.43</b>	<b>2.11</b>
<b><math>\gamma'</math></b>	<b>73.84</b>	<b>8.65</b>	<b>3.34</b>	<b>1.49</b>	<b>4.30</b>	<b>6.32</b>	<b>1.49</b>
<b>Sample A</b>							
<b>Matrix <math>\gamma</math></b>	<b>66.02</b>	<b>11.23</b>	<b>7.69</b>	<b>1.1</b>	<b>2.47</b>	<b>4.47</b>	<b>1.03</b>
<b>Eutectic</b>	<b>71.25</b>	<b>10.14</b>	<b>5.42</b>	<b>1.3</b>	<b>3.1</b>	<b>5.88</b>	<b>0.92</b>
<b><math>\gamma'</math></b>	<b>74.00</b>	<b>9.05</b>	<b>3.22</b>	<b>1.73</b>	<b>3.8</b>	<b>6.54</b>	<b>0.87</b>
<b>Sample B</b>							
<b>Matrix <math>\gamma</math></b>	<b>66.02</b>	<b>12.98</b>	<b>7.09</b>	<b>0.80</b>	<b>2.03</b>	<b>4.52</b>	<b>0.98</b>
<b>Eutectic</b>	<b>69.58</b>	<b>10.97</b>	<b>6.52</b>	<b>1.43</b>	<b>2.99</b>	<b>5.56</b>	<b>0.78</b>
<b><math>\gamma'</math></b>	<b>74.72</b>	<b>9.14</b>	<b>3.1</b>	<b>1.88</b>	<b>4.28</b>	<b>6.46</b>	<b>0.65</b>
<b>Sample C</b>							
<b>Matrix <math>\gamma</math></b>	<b>66.82</b>	<b>11.38</b>	<b>8.05</b>	<b>0.89</b>	<b>2.32</b>	<b>4.38</b>	<b>1.05</b>
<b>Eutectic</b>	<b>70.24</b>	<b>10.48</b>	<b>6.00</b>	<b>1.25</b>	<b>2.85</b>	<b>5.66</b>	<b>0.98</b>
<b><math>\gamma'</math></b>	<b>77.07</b>	<b>8.96</b>	<b>2.99</b>	<b>1.63</b>	<b>3.66</b>	<b>6.16</b>	<b>0.96</b>
<b>Sample D</b>							
<b>Matrix <math>\gamma</math></b>	<b>67.13</b>	<b>11.11</b>	<b>8.16</b>	<b>1.18</b>	<b>2.17</b>	<b>4.34</b>	<b>1.05</b>
<b>Eutectic</b>	<b>70.67</b>	<b>10.24</b>	<b>6.34</b>	<b>1.52</b>	<b>3.2</b>	<b>5.18</b>	<b>0.78</b>
<b><math>\gamma'</math></b>	<b>74.44</b>	<b>9.5</b>	<b>3.63</b>	<b>1.77</b>	<b>4.19</b>	<b>6.47</b>	<b>0.56</b>
<b>Sample E</b>							
<b>Matrix <math>\gamma</math></b>	<b>61.61</b>	<b>10.98</b>	<b>7.22</b>	<b>0.74</b>	<b>1.62</b>	<b>4.30</b>	<b>6.06</b>
<b>Eutectic</b>	<b>70.95</b>	<b>9.92</b>	<b>5.46</b>	<b>1.45</b>	<b>3.51</b>	<b>5.47</b>	<b>0.32</b>
<b><math>\gamma'</math></b>	<b>73.94</b>	<b>8.57</b>	<b>3.36</b>	<b>1.68</b>	<b>4.23</b>	<b>6.67</b>	<b>1.02</b>

The thermal conductivity,  $\kappa$ , can be considered to be due to electron or lattice vibrations, the latter even referred to as phonon conduction. According to Debye [18], the thermal diffusivity can be expressed by the equation:

$$\kappa = \frac{1}{3} n C_v v l \quad (2)$$

where  $n$  is the number of particles per unit volume,  $C_v$  is the heat capacity at constant volume per particle (so that  $nC_v$  is the heat capacity per unit volume expressed in  $\text{J.K.m}^{-3}$ ),  $v$  the velocity of sound and  $l$  is the mean free path [19, 20]. Assuming that the velocity of sound  $v$  is constant, the thermal conductivity will be proportional to electrons or phonons mean free path. The term  $l$  is dependent on collision between electrons or phonons as well as with lattice defects.

The thermal diffusivity measurements of samples A-D, quenched from different temperatures show almost same value. This value is close to the thermal diffusivity of the raw sample at room temperature. It can be observed that the positive temperature dependence of thermal diffusivity shown in **Figure 8** is independent of microstructure below 1223 K. The thermal conductivity in **Figure 9** was found to increase with temperature and can be considered as proportional to  $T^n$ . If  $l$  is independent of  $T$ , the thermal conductivity will be proportional to  $C_v$ , which, in turn, is approximately proportional to  $T^3$  [20]. The situation in the present case is complicated due to the industrial sample being investigated, where the precipitation of intermediate phases like  $\text{Ni}_3\text{Al}$  ( $\gamma'$  phase) might not have reached equilibrium state.

At later stages, in the temperature range 1223 K to solidus temperature, the thermal diffusivity in **Figure 8** as well as the thermal conductivity in **Figure 9** show constancy or a slight decrease with temperature. This could be that, in this range of temperatures, the intermediate phases, which have nucleated, started to dissolve in the matrix. The variation of thermal diffusivity/conductivity with temperature can be attributed to a) in the presence of  $\gamma'$  phase, the electrical resistivities increased and as a result the thermal conductivity decreased. On the other hand, the coarsening of this phase by increasing temperature causes decreasing of electrical resistivity and as a result, increasing of the thermal conductivity [21]. At this temperature range, the mixing of these two mechanisms can cause the constancy or a slight decreasing of thermal conductivity b) as the impurity level in the matrix increases due to the dissolution  $\gamma'$  phases, the disorder of the alloy increases, the mean free path decreases c) part of the heat energy supplied by the laser shot is absorbed at phase transformation *viz.* the dissolution of  $\gamma'$  phase. **Figure 8** shows that there is no significant change in the thermal diffusivity values after annealing during isothermal measurements at 1277, 1403 and 1531 K as a function of time or temperature and that the values obtained after annealing are lower than those measured without annealing treatment. This is indicative of the attainment of thermodynamic equilibrium, where the dissolution of the intermediate phases in the matrix might have been complete and the attainment of impurity levels in the matrix was in maximum.

In liquid state, the average value was  $0.058 \text{ cm}^2/\text{s}$  and it can be seen that there is no significant change with increasing temperature. It may be attributed to the decrease of the mean free path being shorter than characteristic distance between two neighboring atoms.

It is admitted that the present thermal diffusivity values in liquid state could be affected by a certain degree of convection (the upper liquid surface was 2 K higher than the bottom and thus the convective force has to work against gravity) as well as the free liquid surface between the crucibles, which was about 12% of the total sample surface as shown in **Figure 11**.

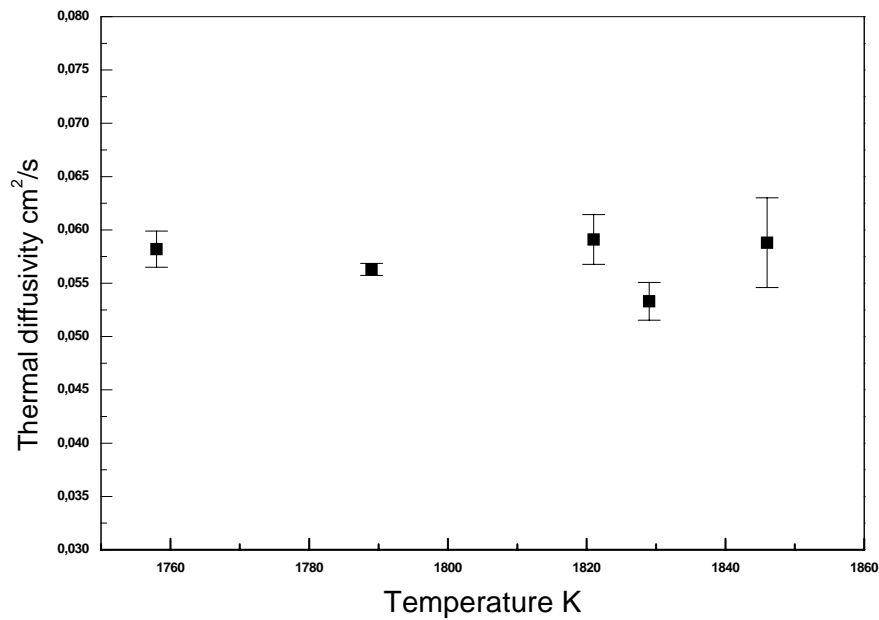


**Figure 11.** Results of Thermal diffusivity measurements in the case of liquid CMSX-4 alloy.

### 3.1.2. 90Ti.6Al.4V alloy

Thermodynamic stabilities of this alloy under investigation at various temperatures were carried out with the help of Thermo Calc software. **Figure 12** shows the phase diagram of the alloy used in the present work, computed using this software. It can be seen that the material contains bcc+hcp+ $\text{Ti}_3\text{Al}$  ( $\gamma'$  phase) at temperatures below 1203 K. Above this temperature, only bcc phase is stable and the  $\gamma'$  phase dissolves into the metal matrix. According to **Figure 12**, the solidus temperature is 1965 K and liquidus temperature is 1971 K.

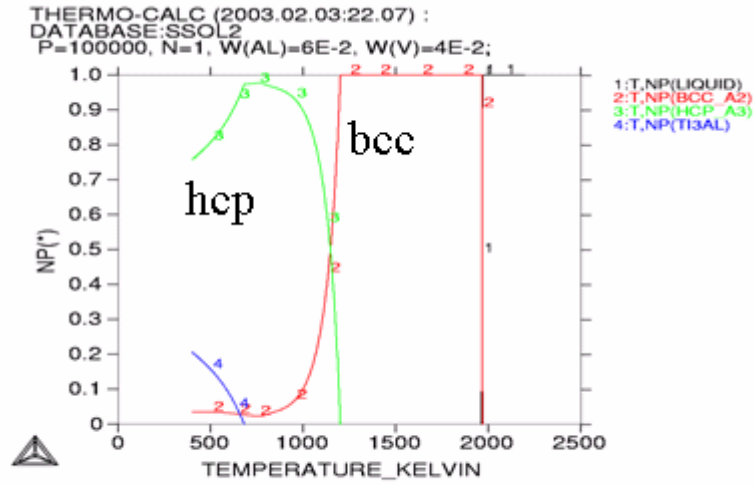


**Figure 12.** Calculated phase diagram of 90Ti.6Al.4V alloy.

During the thermal diffusivity measurement of 90Ti.6Al.4V alloy, the samples were heated to 1673 K and cooled to room temperature at the rate of 6 K.min<sup>-1</sup>. Microscopic observations showed that the sample surface was found to be rough after the annealing at high temperatures owing to the grain growth. Consequently, it was considered that the data obtained during the cooling cycle were not reliable and ignored in trials 1, 2 and 3. In order to study the effect of the thermal history of the alloy, in trial 4, the sample was kept at 1650 K for 11h, cooled in the furnace and polished to make the surface smooth. In this particular case, the thermal diffusivity measurements were carried out during heating and cooling cycles.

**Figure 13** shows the experimental results of the thermal diffusivity measurements as a function of temperature of 90Ti.6Al.4V. The stability regions of the various phases in the 90Ti.6Al.4V have been presented along with the thermal diffusivity values in this figure.

It is seen that the thermal diffusivity increases with temperature below 1225 K. This might be due to the fact that the mean free path might be increasing with temperature. It can also be observed that the sample annealed at 1649 K for 11 hours (sample 4) has lower thermal diffusivity compared to the non annealed samples. This difference is attributed to the difference in the annealing history of the sample. A slight decreasing and/or constancy of thermal diffusivity was observed above 1223 K. In this region, the intermediate phase, Ti<sub>3</sub>Al, dissolves in the matrix to varying extents causing an increase in the disorder in the structure of the sample.

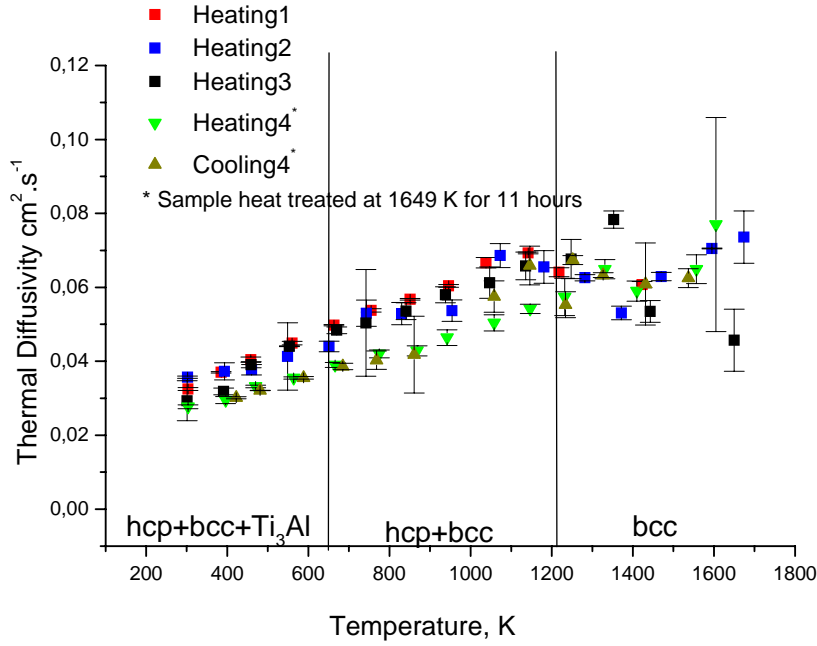


**Figure 13.** Thermal diffusivity- temperature curves of 90Ti.6Al.4V alloy.

The estimated thermal conductivities using equation (1) of 90Ti.6Al.4V alloy were calculated from the present results and the literature values of  $C_p$  and  $\rho$  [22]. The thermal conductivity as a function of temperature was plotted in **Figure 14**.

Mills [22] has earlier presented a model for estimating the thermal conductivity of titanium alloys using the following equations:

$$298 \leq T \leq 973 \text{ K: } \kappa_T = \kappa_{298} + (23 - \kappa_{298}) * (T - 298) / 657 \quad (3)$$

$$973 \leq T \leq 1273: \kappa_T = 15.2 + 0.0273 (T - 973) \quad (4)$$

$$1273 \leq T \leq 1923: \kappa_T = 23 + 0.0075 (T - 1273) \quad (5)$$

In order to use the equations, it is necessary to incorporate the values for the thermal conductivity at room temperature. In the present calculations, the results obtained at room temperature in this work were used. The experimental results obtained are compared with those obtained by using Mills equation in **Figure 14**.

In this case, the agreement with the experimental values is satisfactory in the entire temperature range of the measurements. Thermal conductivity values of the pure components reported by [22] and [23] have also been shown in same figure for comparison. It is seen that the thermal conductivity values are very close to those of pure Ti.

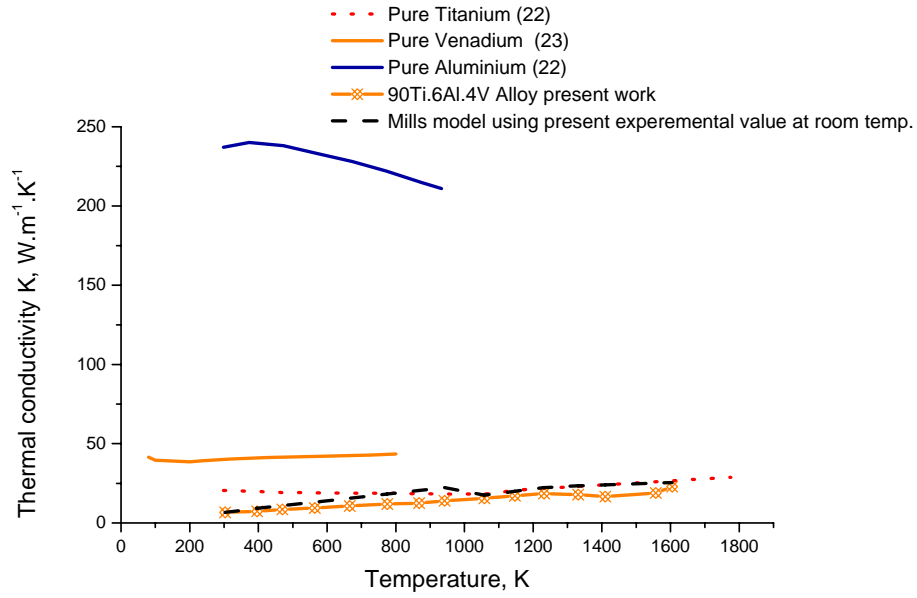


**Figure 14.** Thermal conductivity of 90Ti. 6Al. 4V alloy compared with thermal conductivity calculated by Mills model using the experimental value at room temperature as a start value.

### 3.1.3. 25Cr:6Ni stainless steel

**Figure 15** shows the computed phase diagram of stainless steel alloy. It can be seen that the material contains bcc + fcc +  $\sigma$  below 928 K. Between 928 and 1171 K, fcc and  $\sigma$  phases are stable and fcc + bcc phases are stable between 1171 K and solidus temperature, which is 1615 K. Thus, the  $\sigma$  phase (FeCr) is stable in the temperature interval between room temperature and 1218 K. The liquidus temperature is 1717 K.



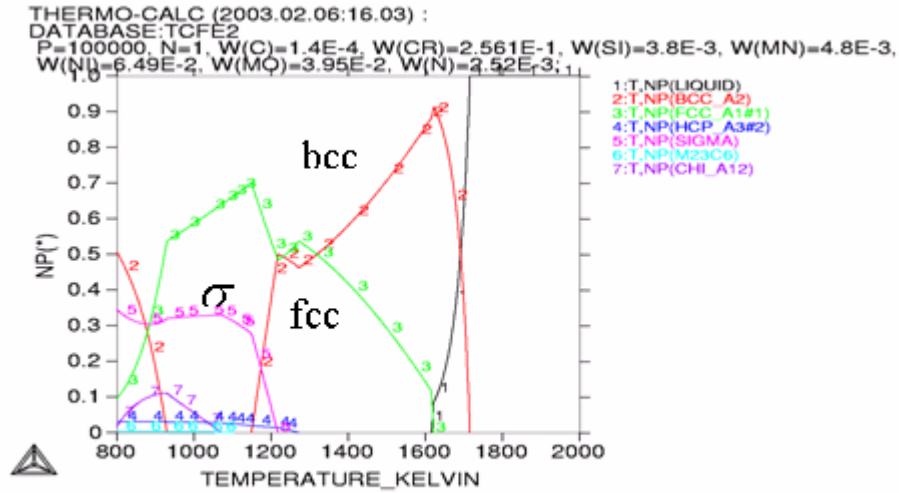


**Figure 15.** Calculated phase diagram of 25Cr:6Ni stainless steel.

**Figure 16** shows the temperature dependence of the thermal diffusivity of stainless steel sample. The phases predicted by the thermodynamic computation are marked in the figure as well. It can be seen that the thermal diffusivity is nearly constant up to about 700 K. Beyond this temperature, there is an increase of the thermal diffusivity with increasing temperature. These results are in agreement with that of AISI 301 and AISI 304 austenitic stainless steel, which are nonmagnetic materials [24]. The data obtained during the cooling cycle is almost identical to that during heating cycle. It means that the effect of  $\sigma$  phase on the thermal diffusivity is negligible in this temperature range. The increase in the slope of the curve above 950 K can be due to increase in the bcc portion in the structure.

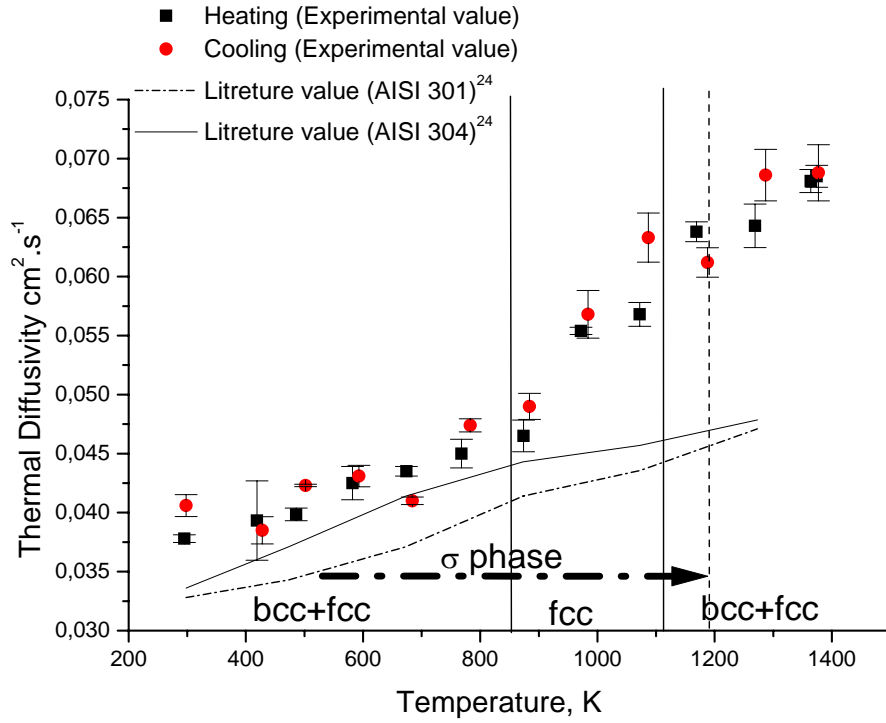


**Figure 16.** Thermal diffusivity-temperature curves of stainless steel.

The estimated thermal conductivities of 25Cr:6Ni stainless steel based on equation (1) were found to be in good agreement with the thermal conductivity of the same alloy used Mills model, which used equations (6) and (7) to determine the thermal conductivity of steel. This agreement can be seen clearly in **Figure 17**. It should be pointed out that the experimental thermal conductivity value at room temperature obtained in the present investigation was used as a start value of Mills model.

$$298 \leq T \leq 1073 \text{ K:} \quad \kappa_T = \kappa_{298} + (25 - \kappa_{298}) * (T - 298) / 775 \quad (6)$$

$$1073 \leq T \leq 1573 \text{ K:} \quad \kappa_T = 25 + 0.013 (T - 800) \quad (7)$$

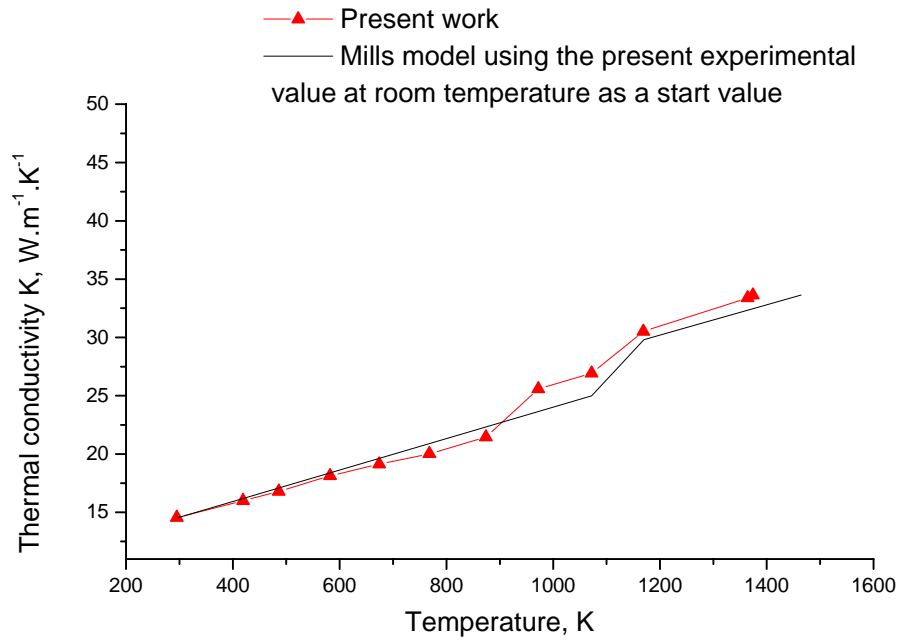


**Figure 17.** Thermal conductivity of stainless steel compared with thermal conductivity calculated by Mills model using the experimental value at room temperature as a start value.

#### 3.1.4. 0.7% carbon steel

**Figure 18** shows the phase diagram of high carbon steel used in present work. It can be seen that the material contains bcc phase at temperature below 954 K. Between 954 and 1026 K bcc + fcc phases are stable. Above this temperature, fcc phase is stable until the solidus temperature, which is 1638 K. The figure also shows that the liquidus temperature is 1746 K.

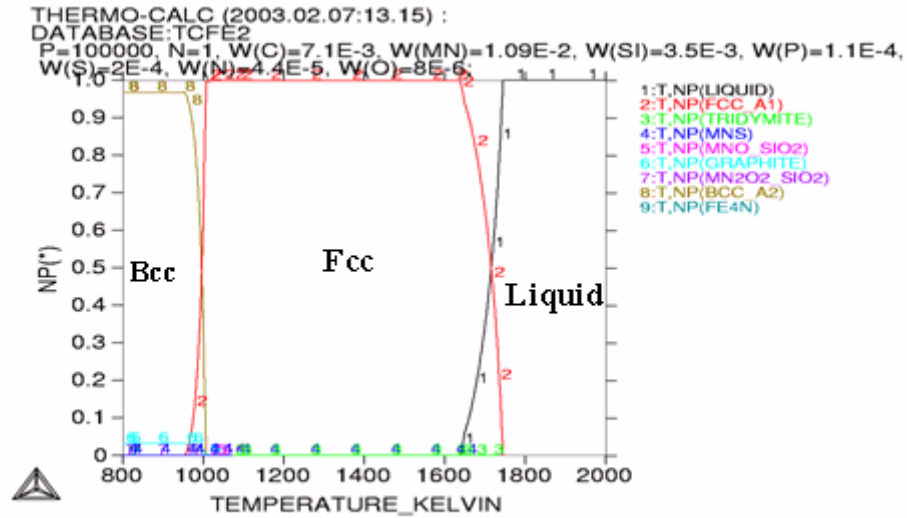


**Figure 18.** Calculated phase diagram of 0.7%C Steel.

**Figure 19** shows the thermal diffusivity measurement results obtained in the case of 0.7% carbon steel as a function of temperature. The figure shows that the thermal diffusivity of the plain carbon steel sample decreases with increasing temperature where the microstructure contains bcc phase. The corresponding values for Armco iron, taken from literature [25] show a similar trend. The minimum thermal diffusivity values can be observed at 970 K (Curie point). If a ferromagnetic transition exists in a metal, thermal diffusivity always decreases from room temperature to the Curie temperature, as the disorder increases [25,26,27]. Beyond this point, thermal diffusivity shows an increase.

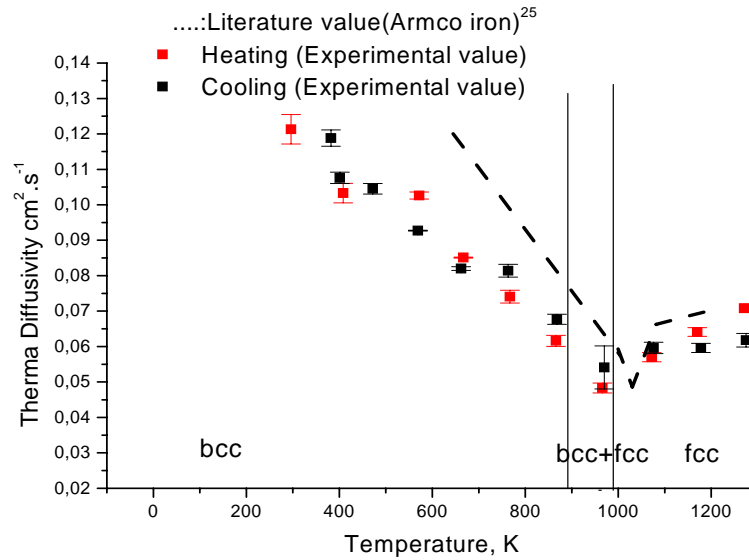


**Figure19.** Thermal diffusivity-temperature curves of 0.7% carbon steel.

The estimated thermal conductivity of 0.7% carbon steel based to equation (1) was found to be in good agreement with the thermal conductivity of the same steel used Mills model, obtained from equations (6) and (7) using the present experimental thermal conductivity value at room temperature used as a start value of Mills model. This agreement can be seen clearly in **Figure 20**.

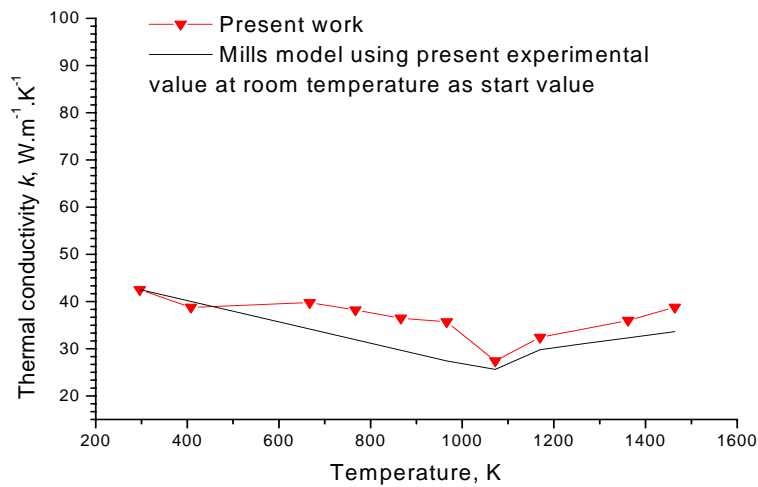


**Figure 20.** Thermal conductivity of 0.7% carbon steel alloy compared with thermal conductivity calculated by Mills model using the present experimental value at room temperature as a start value.

### 3.1.5. Electron contribution of thermal conduction of alloys

The thermal conductivity of the metals and alloys is composed of two components: a lattice component  $k_g$  and electronic component  $k_e$ . In both cases, heat is transported by mobile carriers. Weidman-Franz-Lorenz formula has been used to calculate the thermal conductivity using electrical resistivities of the alloys similar in composition to the above-mentioned alloys at room temperature [21, 28]. The aim of this calculation is to estimate the contribution of the electron as heat conductor in these alloys. The relevant equation is

$$\kappa / \sigma_e \cdot T = 2.45 \cdot 10^{-8} \text{ W} \cdot \Omega \cdot \text{K}^{-2} \quad (8)$$

Where  $\kappa$  is the thermal conductivity  $\text{W} \cdot \text{m}^{-1} \cdot \text{K}^{-1}$ ,  $\sigma_e$  is the electrical conductivity  $\Omega^{-1} \cdot \text{m}^{-1}$  and  $T$  is the absolute temperature (Kelvin). **Table V** shows the calculated and measured thermal conductivity of above mentioned alloys.

**Table V.** Calculated electrical conductivity and measured thermal conductivity of alloys used in present work.

Material	Electrical conductivity $\Omega \cdot \text{m}^{-1}$	Calculated thermal conductivity $\text{W} \cdot \text{m}^{-1} \cdot \text{K}^{-1}$	Measured thermal conductivity $\text{W} \cdot \text{m}^{-1} \cdot \text{K}^{-1}$	Electron contribution %
CMSX-4	$65.13 \cdot 10^4$	4.755	7.807	61
90Ti.6Al.4V	$50.7 \cdot 10^4$	3.7	6.68	55.4
25Cr:6Ni stainless steel	$86.2 \cdot 10^4$	6.3	14.55	43.3
0.7% carbon steel	$57.4 \cdot 10^5$	41.9	42.50	98.6

It can be seen that the addition of Cr to the steel decreases the electronic contribution from 98.6% to 43.3%. On the other hand, the presence of  $\text{Ti}_3\text{Al}$  in the titanium alloy as well as  $\text{Ni}_3\text{Al}$  in CMSX-4 alloy cause a lowering of the electrical conductivity as well as electron contribution to the thermal conductivity of these alloys. The electrical conductivity of pure nickel and titanium are  $125 \cdot 10^5$  and  $180 \cdot 10^4$  respectively [28].

### 3.2. Composites

Compositions of various AISI 304 Stainless steel- alumina composites used in this study and their densities,  $\rho$ , are presented in **Table VI**. It can be seen that the density of the specimens decreases with increasing the alumina content.

**Table VI.** Densities of AISI 304 stainless steel-alumina composites.

Sample SS <sub>xx</sub> *	Reference	SS0	SS0.001	SS0.01	SS0.1	SS1	SS2	SS3	SS5	SS7	SS8	SS10
Density kg/m <sup>3</sup> *10 <sup>3</sup>	7.6	7.54	7.58	7.57	7.51	7.43	7.43	7.29	7.18	7.12	6.639	6.609

\* The number beside SS refers to the Al<sub>2</sub>O<sub>3</sub> wt% content in the sample composition.

Typical SEM micrographs taken from polished cross-sections of Stainless steel-alumina composites are shown in **Figure 21**. It can be seen that the alumina particles are uniformly dispersed through the material at low alumina contents. No appreciable deformation or microcracks of adjoining grains in the composites, which might occur due to thermoelastic mismatch between the stainless steel and the alumina particles, could be detected. At higher alumina contents, a tendency of alumina particles to agglomerate is evident.

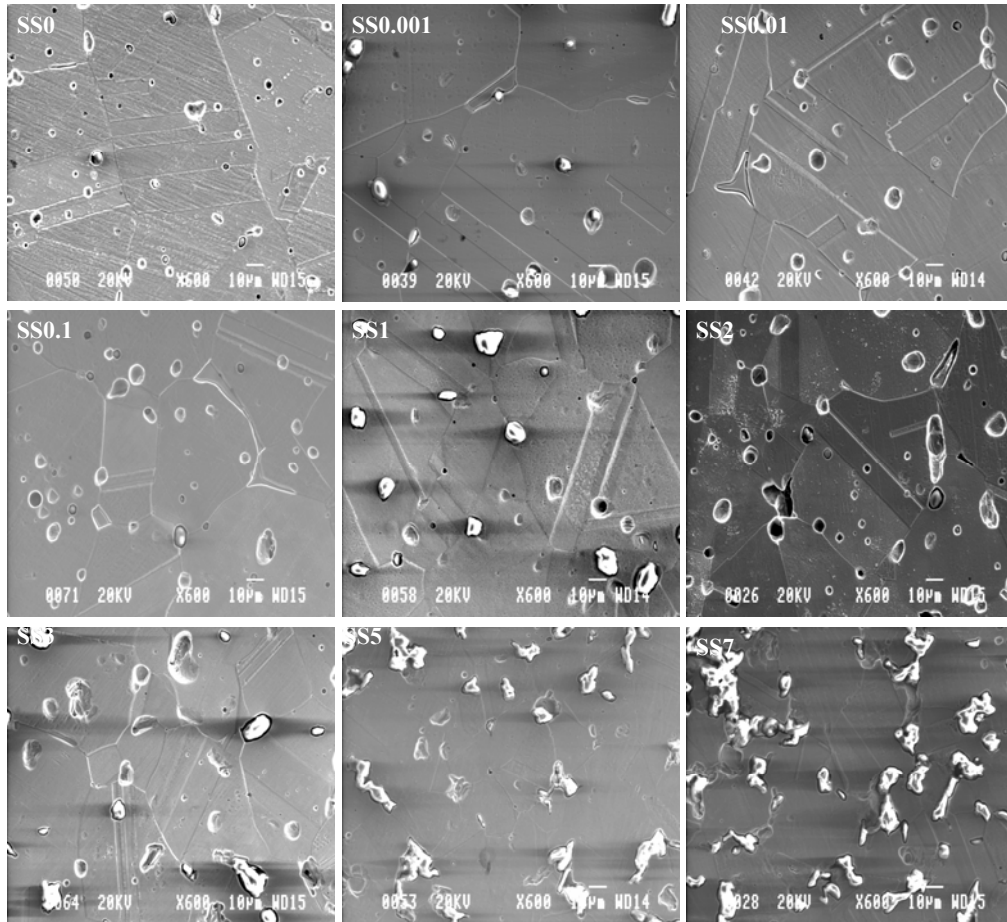


**Figure 21.** SEM micrograph of polished cross-sections of AISI 304 Stainless steel-alumina composite containing various alumina wt%.

Thermal diffusivities of cold pressed and sintered specimens of AISI 304 stainless steel-alumina composites of various compositions, as a function of temperature, are shown in **Figure 22**.



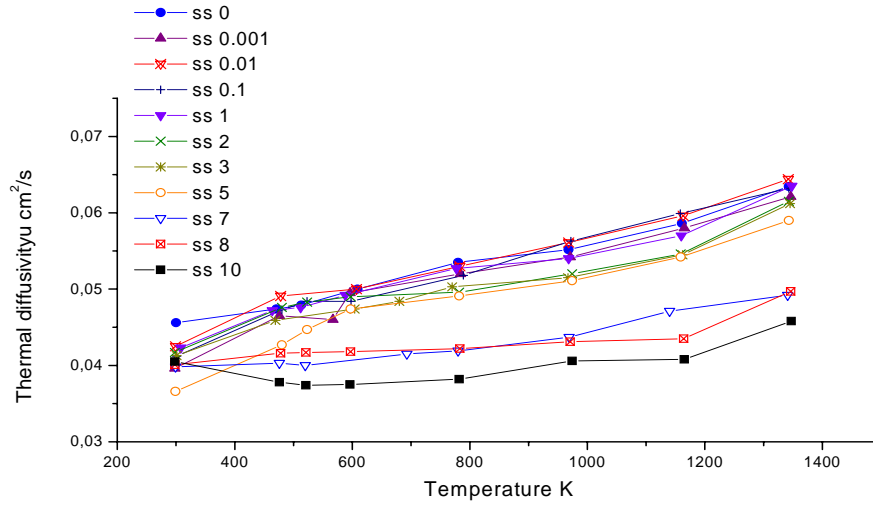


**Figure 22.** Temperature dependence of thermal diffusivity of Stainless steel-alumina composite containing (0-10) wt% alumina.

The thermal conductivities of the specimens, investigated in the present work could be calculated using simple rule of mixture at every temperature from experimental thermal diffusivities, the values of the heat capacity reported by [29] and density according to equation (1). The thermal conductivities thus computed are presented in **Figure 23**.

It can be seen that the thermal diffusivity as well as thermal conductivity of specimens increase with the temperature as shown in **Figures 22** and **23**. This tendency could be due to increase of the electron-electron mean free path with increasing temperature. These results are in agreement with that of austenitic stainless steel, which is a nonmagnetic material as reported by Westover [30]. **Figure 23** also shows that there is no significant change of the thermal conductivity with increasing alumina content in the range between 0 and 5 wt% alumina. Above that, the thermal conductivity decreases with increasing the alumina content. This trend is clearer at high temperatures. At lower temperatures, the combination of the two opposing effects, *viz.*, decrease in the thermal conductivity due to increase of alumina content, which is an insulator to the electron transport and the increase due to increase in the thermal conductivity of alumina itself might be plausible reasons.

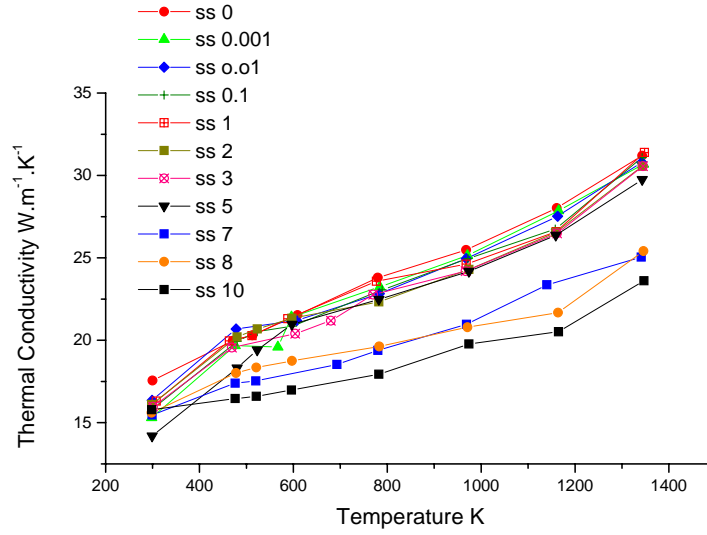


**Figure 23.** Temperature dependence of thermal conductivity of Stainless steel-alumina composite containing (0-10) wt% alumina.

The thermal conductivity as a function of the alumina content at 970 and 1162 K is plotted in **Figures 24** and **25** respectively. No evidence of difference between the trends of the values between these two figures could be noted. This might be due to the same behavior of the electrons transport at these temperatures.

In this study, simple rule of mixture reported by James et al [31], Eucken equation reported by Hayashi et al [32], and Ohm's law model developed by Hayashi et al [33] have been used to compare the measured values with these models as shown in **Figures 24** and **25**.

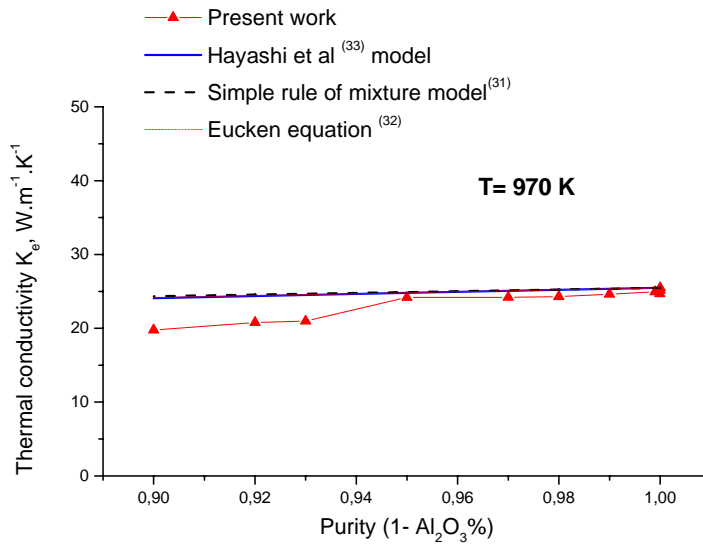


**Figure 24.** Effect of the alumina content on the thermal conductivity of stainless steel-alumina composite at 970 K compared to previous models.

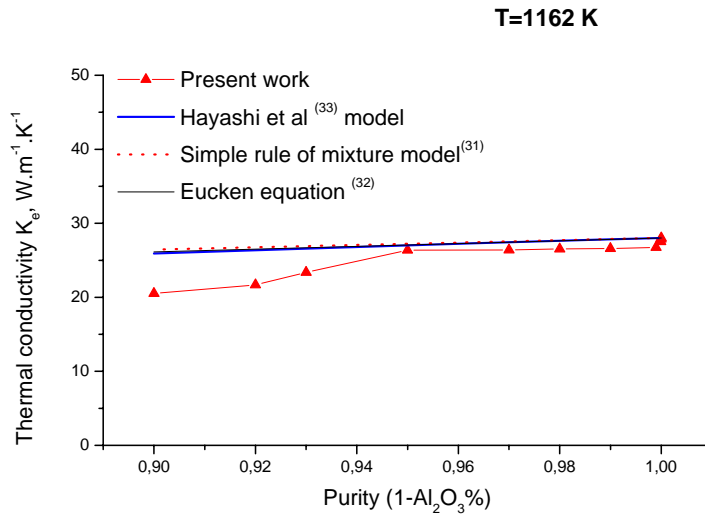


**Figure 25.** Effect of the alumina content on the thermal conductivity of stainless steel-alumina composite at 1162 K compared to the previous models.

In the simple rule of mixture, the thermal conductivity of the composites ( $\kappa_c$ ) can be written as follows:

$$\kappa_c = (\kappa_{st.st} * \chi_{st.st}) + (\kappa_{Al_2O_3} * \chi_{Al_2O_3}) \quad (9)$$

where  $\kappa_c$ ,  $\kappa_{st.st}$  and  $\kappa_{Al_2O_3}$  represent the thermal conductivity of composites, stainless steel and alumina respectively and  $\chi_{st.st}$ ,  $\chi_{Al_2O_3}$  are the weight fraction of stainless steel and alumina.

On the other hand, the thermal conductivity of a binary phase material  $\kappa_c$  generally obeys the Eucken relationship, when a minor amount of discontinuous second phase disperses uniformly in a continuous phase. Eucken equations are:

$$K_c = \frac{\kappa_{st.st} (1 + 2\phi_{Al_2O_3} \cdot A)}{(1 - \phi_{Al_2O_3} \cdot A)} \quad (10)$$

where  $\phi_{Al_2O_3}$  is the weight fraction of alumina and

$$A = \frac{1 - (\kappa_{st.st} / k_{Al_2O_3})}{(2K_{st.st} / k_{Al_2O_3}) + 1} \quad (11)$$

Furthermore, The Ohm's law model developed by Hayashi et al, introduces the finite transverse heat flow, i.e., in X and Y direction as shown in **Figure 26**.

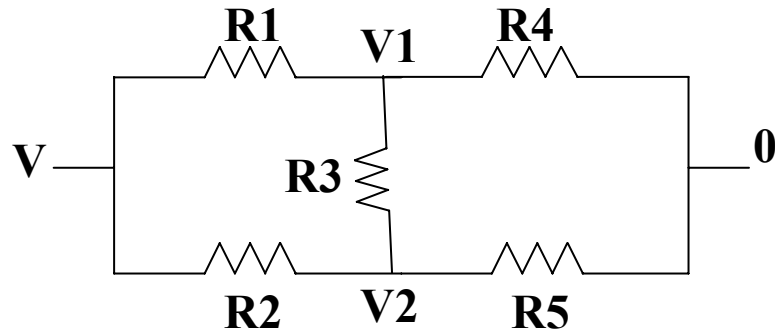
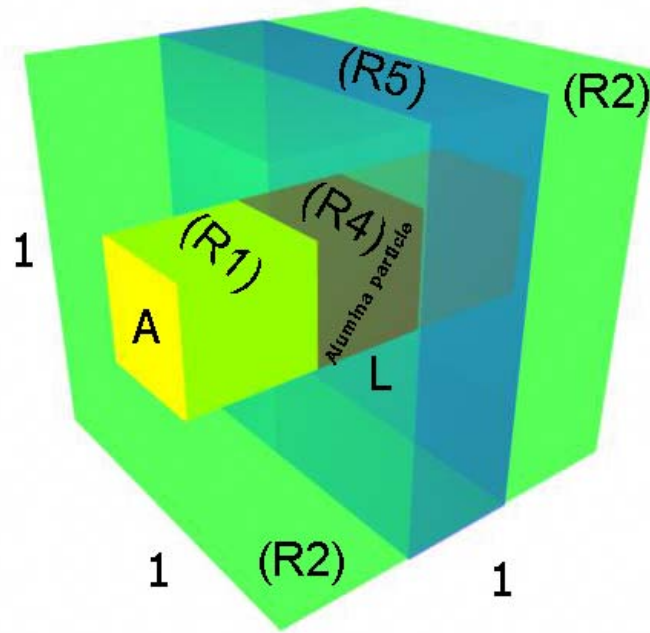


**Figure 26.** Simple Ohm's law model including the finite transverse heat flow [33].

This model considers that the effective thermal conductivity  $K_c$  of the composites corresponding to the reciprocal of the five-resistor circuit. The value of  $K_c$  can be written by applying Ohm's law:

$$K_c = (V1/R4 + V2/R5) \quad (12)$$

here the value of  $R1, R2, R3, R4$  and  $R5$  can be written as follows:

$$R1=(1-L)/(AK_s) \quad (13)$$

$$R2=(1-L)/((1-A)K_s) \quad (14)$$

$$R3=1/[4(1-L)K_s] \quad (15)$$

$$R4=L/(AK_f) \quad (16)$$

$$R5=L/((1-A)K_s) \quad (17)$$

where L and A are the length and the cross/ section area of a rectangular alumina particle, respectively. K<sub>s</sub> and K<sub>f</sub> are the thermal conductivity of the matrix and alumina particles respectively.

The Potentials V1 and V2 in the equation (12) and **Figure 26** can be expressed using Kirchhoff's law as follows:

$$V1 = -VR3 \frac{\frac{1}{R2} + \frac{R3}{R1} \left( \frac{1}{R2} + \frac{1}{R3} + \frac{1}{R5} \right)}{1 - R3^2 \left( \frac{1}{R1} + \frac{1}{R3} + \frac{1}{R4} \right) \left( \frac{1}{R2} + \frac{1}{R3} + \frac{1}{R5} \right)} \quad (18)$$

$$V2 = -VR3 \frac{\frac{1}{R1} + \frac{R3}{R2} \left( \frac{1}{R1} + \frac{1}{R3} + \frac{1}{R4} \right)}{1 - R3^2 \left( \frac{1}{R2} + \frac{1}{R3} + \frac{1}{R5} \right) \left( \frac{1}{R1} + \frac{1}{R3} + \frac{1}{R4} \right)} \quad (19)$$

**Figure 24** and **25** show that all the three mentioned models are almost overlapping on each other. They are also in good agreement with the present experimental values, when the weight fraction of the alumina is lower than 5wt%. Above this ratio, there large discrepancy can be observed. This discrepancy could be due to the agglomeration of the alumina particles during pressing and sintering. This agglomeration may cause the “leak away” and scattering of the electrons during heat transport, which decreased the thermal conductivity of the composites. Such agglomeration can be seen in **Figure 21**.

### 3.3. Mould powder

#### 3.3.1. XRD measurements

X-ray diffraction profiles of all glassy samples indicate no traces of crystalline phases, indicating that all glassy samples are amorphous from the viewpoint of x-ray diffraction. **Figure 27** shows the x-ray diffraction profiles of the glassy sample (a) and the samples annealed at 1073 K for 1 h (b) and 15 h(c) for powder A. It can be seen that **Figure 27 (a)** corresponds to the glassy structure. On the other hand, in **Figure 27 (b)**, which corresponds to that for the sample annealed at 1073 K for 1 h, two sharp peaks appear together with the hallow pattern due to the amorphous phase. Two sharp peaks may be attributed to nepheline ( $\text{Na}_3\text{KAl}_4\text{Si}_4\text{O}_{16}$ ,  $\text{NaAlSiO}_4$ ). On the other hand, **Figure 27 (c)** shows that the hallow pattern disappears and only sharp peaks are observed for the sample annealed at 1073 K for 15 h, indicating that the sample has been mostly crystallised. Markings have been made at the angles where the diffraction peaks attributed to cuspidine ( $\text{Ca}_4\text{Si}_2\text{O}_7\text{F}_2$ ) and nepheline ( $\text{Na}_3\text{KAl}_4\text{Si}_4\text{O}_{16}$ ,  $\text{NaAlSiO}_4$ ) should be observed.

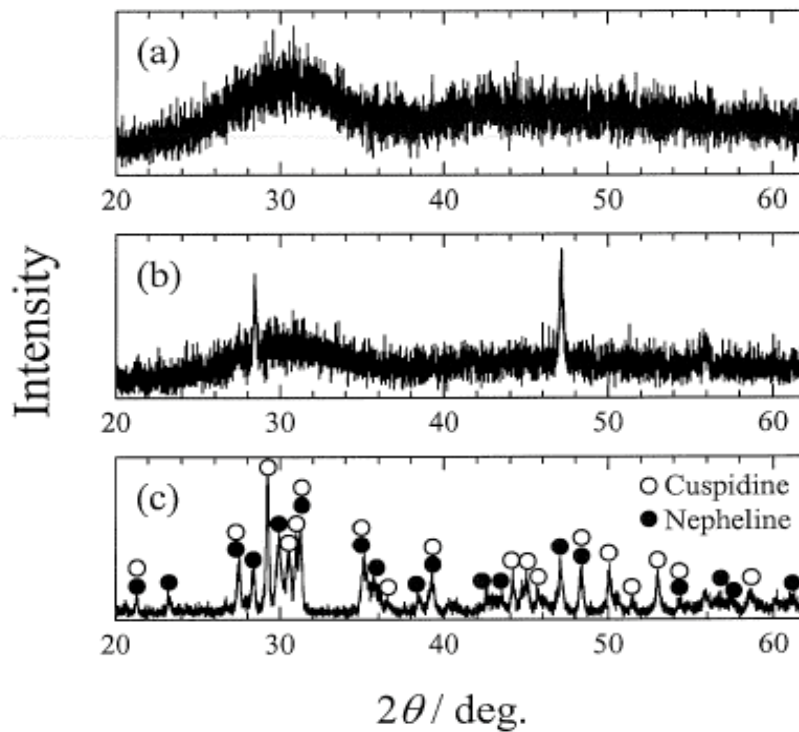


**Figure 27.** X-ray diffraction profiles of the glassy sample(a) and the samples annealed at 1073 K for 1 h(b) and 15 h(c) for powder A.

**Figure 28** shows the X-ray diffraction profiles of the samples annealed at 1073 K for 1 h for powders B-D. Marking has been made at the angles where the diffraction peaks attributed to cuspidine and nepheline should be observed for powder B, and at the angles where the peaks due to cuspidine should be observed for powders C and D.

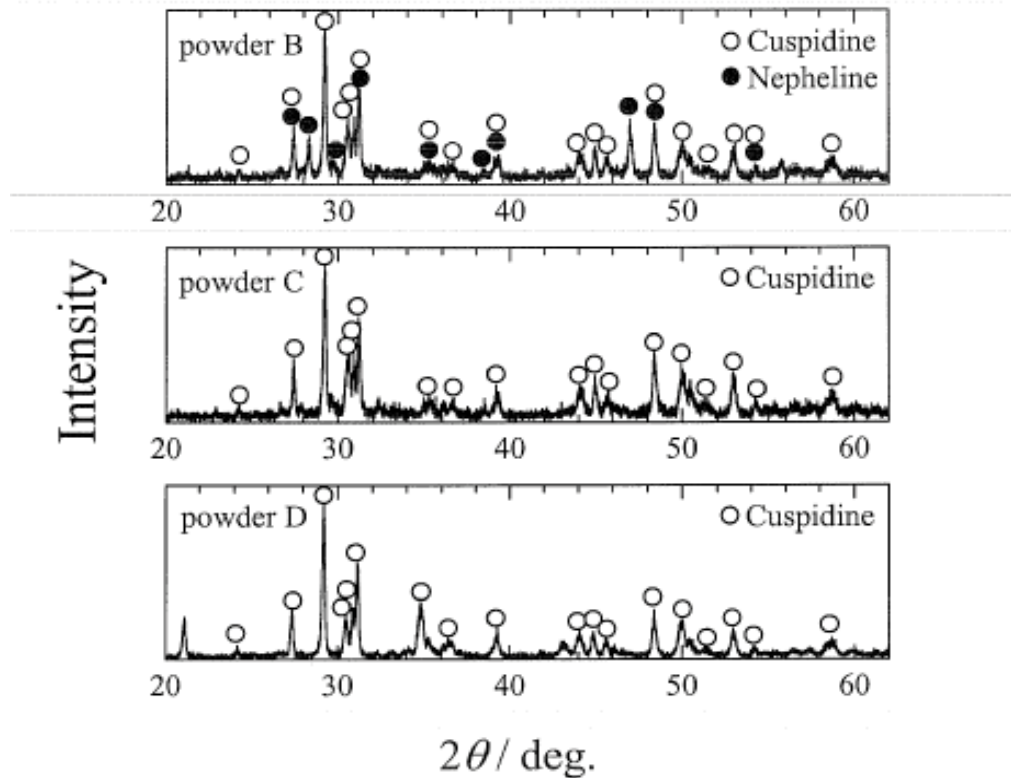


**Figure 28.** X-ray diffraction profiles of the samples annealed at 1073 K for 1 h for powder B-D.

### 3.3.2 Thermal diffusivity measurements

**Figure 29** shows the temperature dependences of the thermal diffusivities of the glassy samples and the samples annealed at 1073 K for 1-120 h for powder A, 1-15 h for powder B and 1 h for powder C and D respectively. Closed symbols are data recorded during the heating cycles and open symbols during the cooling cycles.



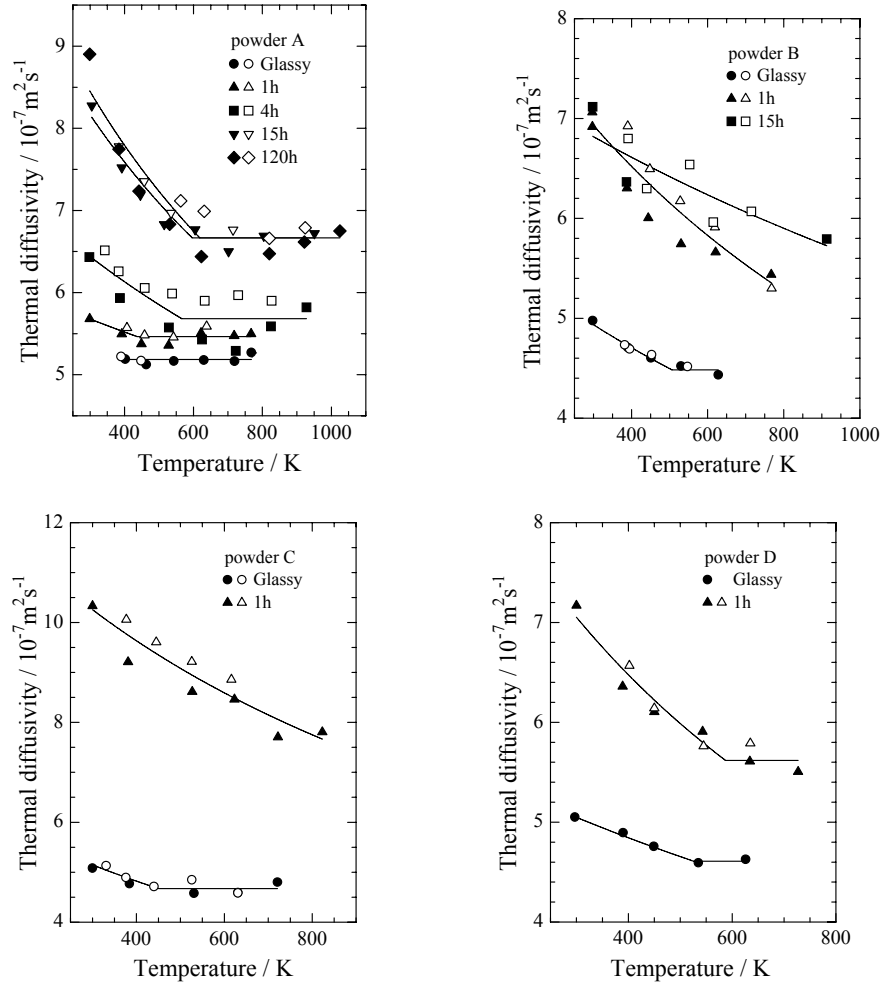


**Figure 29.** Temperature dependencies of the thermal diffusivities of the glassy and crystalline samples for powders B, C and D, respectively.

It can be seen from these figures that the thermal diffusivities of the crystalline samples decrease with increasing temperature at lower temperatures and are roughly constant at higher temperatures. These temperature dependencies were in agreement with those reported by Shibata et al [34]. It can be also seen that the sample annealed for longer time exhibits larger thermal diffusivity in the case of powder A.

Thermal diffusivity is determined by lattice vibration (phonon conduction) in insulators.

Since  $C_v \approx \rho C_p$ , Eqs. (1) and (2) yield, the thermal diffusivity can be describe as the following:

$$\alpha = \frac{1}{3} \nu l \quad (20)$$

If it is assumed that the value of  $\nu$  is constant irrespective of temperature, the thermal diffusivity is proportional to the phonon mean free path. As mentioned earlier, the phonon mean free path is determined principally by two mechanisms, geometrical scattering, i.e., the collisions of phonons with the crystal boundary, lattice imperfections and so on and phonon-phonon interaction. The reciprocal of the effective mean free path  $1/l$  is found by adding the reciprocal of the mean free path for geometrical scattering  $l_{geo}$  and that for phonon-phonon interaction  $l_{p-p}$ , as follows;

$$\frac{1}{l} = \frac{1}{l_{geo}} + \frac{1}{l_{p-p}} \quad (21)$$

Generally, above room temperatures, the geometrical scattering is independent of temperature. On the other hand, the mean free path, determined by phonon-phonon interaction is inversely proportional to temperature above the Debye temperature [18]. Therefore, Eq. (21) is rewritten as

$$\frac{1}{l} = a + bT \quad (22)$$

where  $T$  is the absolute temperature and  $a$  and  $b$  constants. If the temperature is raised to a sufficiently high level, the mean free path decreases to a value near the lattice spacing, and is expected to be independent of temperature [35]. The solid lines in the figures have been drawn based on Eq. (22). **Figure 30** shows the temperature dependencies of the thermal diffusivities of the glassy sample and the samples annealed for 1 h at 1073 and 1173 K for powder A.

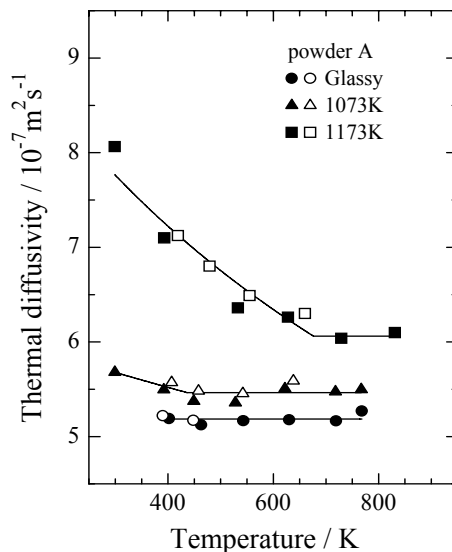


**Figure 30.** Temperature dependencies of the thermal diffusivities of the glassy sample and the samples annealed for 1 h at 1073 and 1173 K for powder A. Closed symbol are data recorded during the heating cycles and open symbols during the cooling cycles.

It can be seen from **Figure 29** that, while the thermal diffusivity of the glassy sample of powder A is constant irrespective of temperature, the thermal diffusivities of the glassy samples of powders B-D decrease with an increase in temperature at lower temperatures and are constant at higher temperatures. It is also found that the constant value of the thermal diffusivity for powders B-D is lower than that of powder A.

Thermal diffusivity of a glassy sample becomes constant independent of temperature when the mean free path is limited to a fixed value by the random network structure. The randomness of the network can be estimated by the ratio of non-bridging oxygen (NBO) atoms / (Si+Al atoms), the ratio being denoted by  $NBO/\tau$  [36]. The  $NBO/\tau$  ratios of powders A, B, C and D can be calculated to be 0.92, 1.48, 1.65 and 2.11, respectively, in the manner proposed by Mills [37] by assuming that fluorine predominantly bonds to calcium rather than other cations [38] and that  $CaF_2$  does not contribute to the breakage of the silicate network [39].

Consequently, the glassy sample of powder A has less random network structure, resulting that the mean free path limited by the network structure is larger than those of other powders. On the other hand, the thermal diffusivities of the glassy samples for powders B-D show roughly the same values of  $4.6 \times 10^{-7} m^2 s^{-1}$  despite of the different  $NBO/\tau$  ratios. As shown in **Figure 31**, the apparent thermal diffusivities of the liquid samples for powders B-D also show similar values, viz.  $4.0 \times 10^{-7} m^2 s^{-1}$ . It is considered that, because the silicate network is largely broken down, there is not a significant change of structure among powders B-D. This tendency has been also shown in the previous data [40].

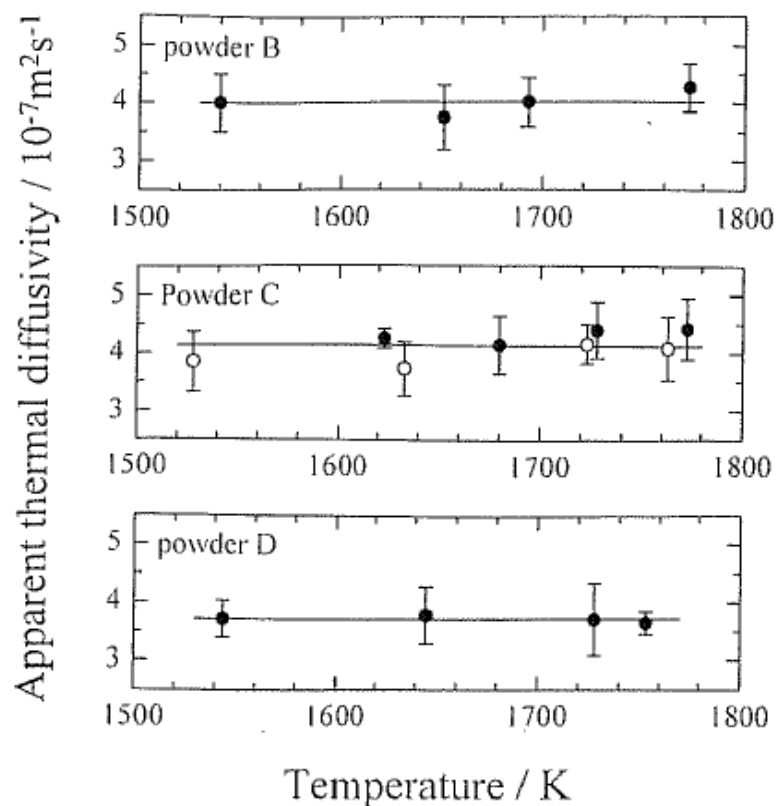


**Figure 31.** Temperature dependencies of the apparent thermal diffusivities of liquid samples of powders B-D.

### 3.4. Coke

#### 3.4.1. XRD measurements

The XRD isothermal measurements of blast furnace coke were carried out at 973, 1073, 1173, 1273, 1373 and 1473 K in order to investigate the effect of time on the degree of graphitisation at these temperatures. **Figure 32** shows the isothermal x-ray diffractograms of coke KL35R at 1273 K. It can be seen that there is no evident change of peaks width as well as intensities i.e. the degree of graphitisation does not change with time. This could be due to the high surface energy of the coke, which gives a sudden phase transformation at high temperature. Similar behaviors were noted in the case of coke KL25C and KL05R in temperature range between 973 and 1473 K. The figure also

shows there is a slight shift of the position of (002) peaks from room temperature and 1273 K. It could be attributed to the thermal expansion of the lattice parameter (d) with increasing temperature.

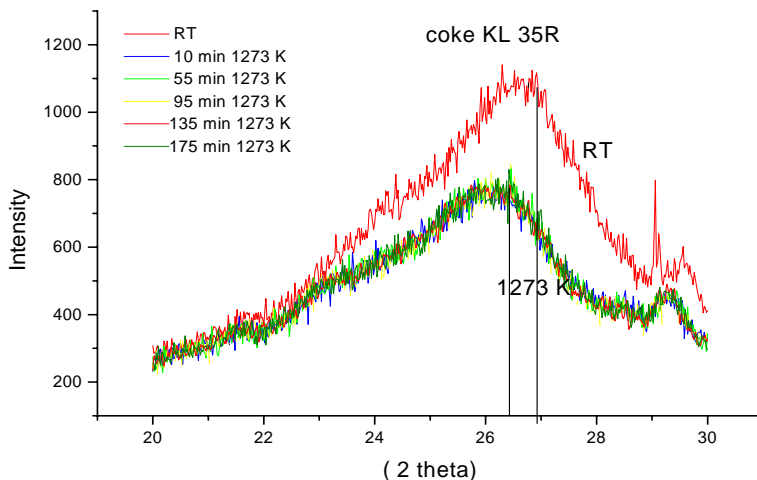


**Figure 32.** X-ray diffractograms of peak (002) during isothermal measurements at 1273 K of coke KL35R.

**Figure 33** shows the XRD diffractograms during non-isothermal measurements of same coke samples. The decrease of maximum intensities of the peaks with increasing temperature could be due to increase the atom and molecules vibration about their equilibrium position, which makes the diffraction intensities weaker [14].

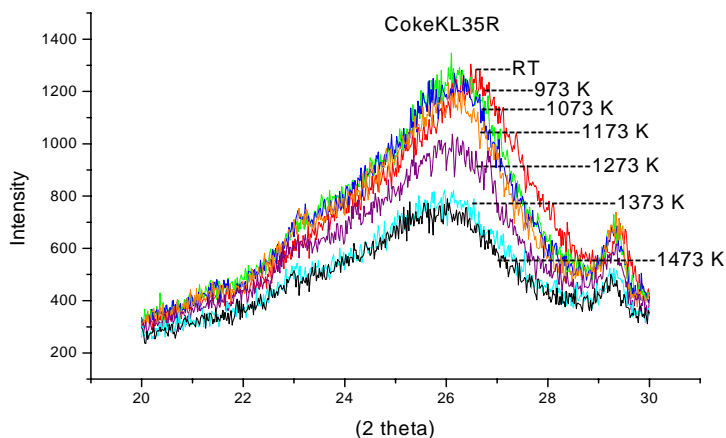


**Figure 33.** XRD diffractograms during non- isothermal measurements of coke KL35R.

The vertical dimension of carbon crystallite  $L_c$  was calculated from XRD data using Scherrer formula:

$$L_c = K \lambda / B \cos \theta \quad (23)$$

Where, K is the shape factor =0.9, B is the width of the peak (002) at half intensity (radian) and  $\theta$  is position of the (002) peak.

**Figure 34** shows the calculated  $L_c$  of non-isothermal XRD diffractograms versus temperature. The figure includes error bar, which are estimated from the calculation of ( $L_c$ ) by using eq. (23). Both the width of the peak as well as the intensity are difficult to establish with high accuracy from XRD plots, especially for amorphous peaks, when there is a higher degree of graphitisation and a lower amount of amorphous carbon in the KL25C and KL35R at high temperature. The figure also shows that ( $L_c$ ) is lower in coke 05R than in coke KL25 and KL35. This may be due to a higher amorphous carbon percentage of coke 05R, which was taken from the top level of blast furnace at 1073 K compared to coke 25C and 35R, which were taken from the lower level at 1623 K, where the amorphous carbon content is lower.  $L_c$  results reported here are in good agreement with those of the same coke samples at room temperature [6,7].

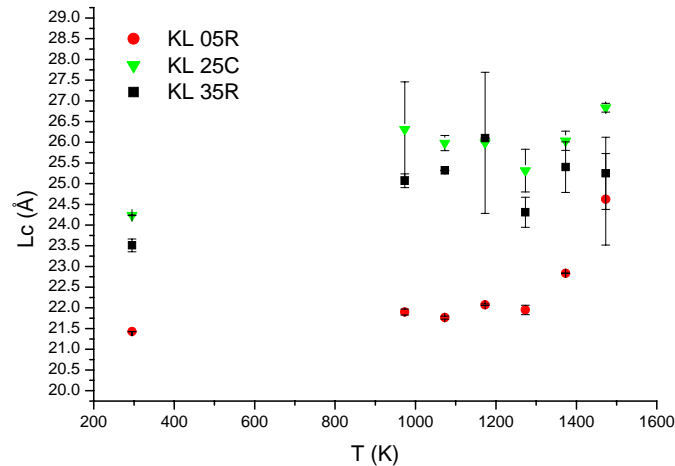


**Figure 34.** Dependence of degree of graphitisation on temperature of EBF coke.

The independence of  $L_c$  with respect to time at temperatures higher than 973 K indicate that the energies associated with the temperature dependence of  $L_c$  are quite low in comparison to the activation energies of graphitisation using TG or DTA of different carbonaceous materials[41, 42]. Graphitisation process consists three stages; a) the first stage consists the elimination of the single interstitial atoms or loops; b) the second stage

includes the energies of C-C breaking and c) third stage consists formation of vacancies and movements of atoms as well as vacancies [43].

The instantaneous transformation observed in present work is caused by the first stage of transformation, which consists the elimination of single interstitial atoms or loop.

**Figure 35** shows that d-spacing increases from room temperature to 973 K for all samples. This is likely to be due to the thermal expansion of the lattice. At temperatures above 973 K, graphitisation occurs, which decreases d-spacing. At the same time, there is thermal expansion due to temperature increase. It is seen in the **Figure 35** that, despite the scatter, final change in d-spacing will be small.

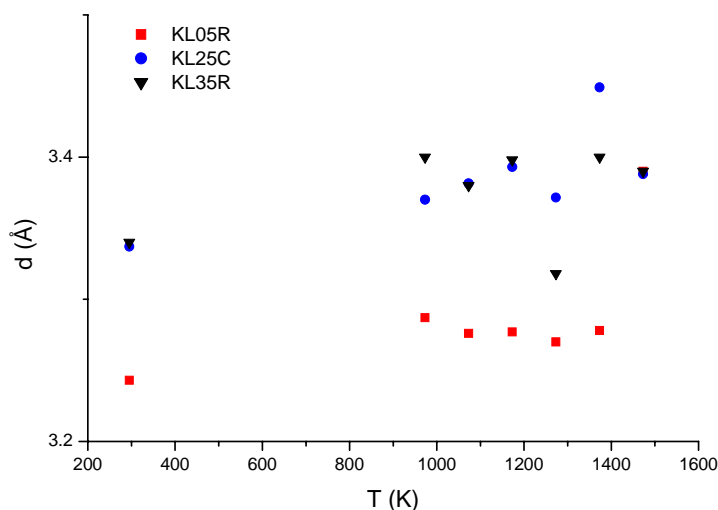


**Figure 35.** The effect of the temperature on inter- layer spacing (d).

### 3.4.2. Heat capacity measurements

Heat capacity as a function of temperature based to the DSC measurements is showing in **Figure 36**. It can be seen that the heat capacity of the coke increases drastically between 973 K and 1400 K.

These results are compared with heat capacity of pure graphite as a function of temperature reported by [29]. The increase observed in the present work could be due to increase the graphitisation degree of the coke with increasing temperature. These results are in good agreement with XRD measurements shown in **Figure 34**.

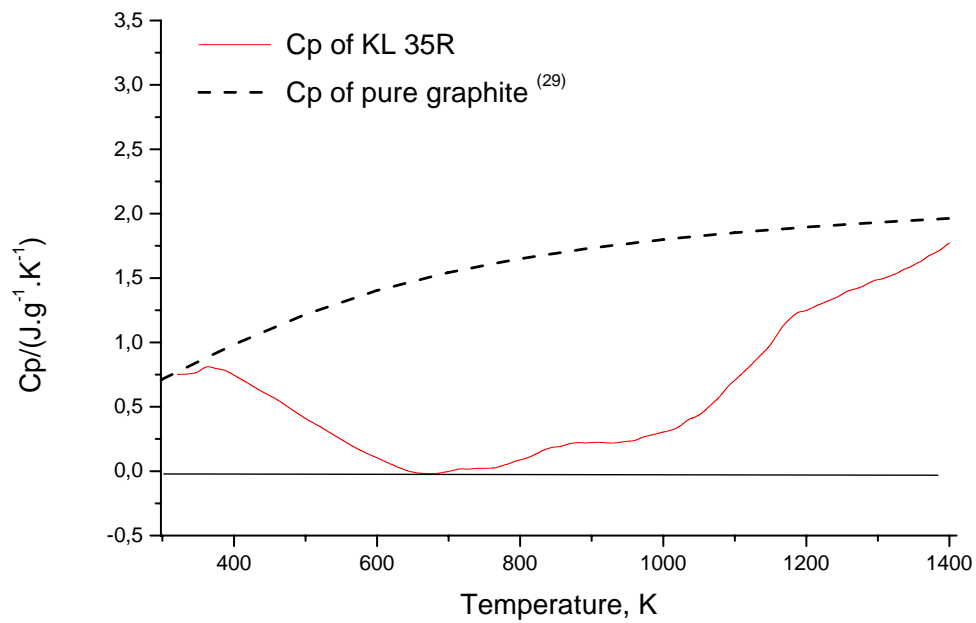


**Figure 36.** Temperature dependence of heat capacity of coke KL 35R compared to the pure graphite heat capacity.

### 3.4.3. Thermal diffusivity measurements

It can be seen from **Figure 37** that the coke samples taken from deeper level of the blast furnace show larger thermal diffusivities. This level dependency of the thermal diffusivity is discussed in terms of the porosity, the degree of graphitisation and ash content.



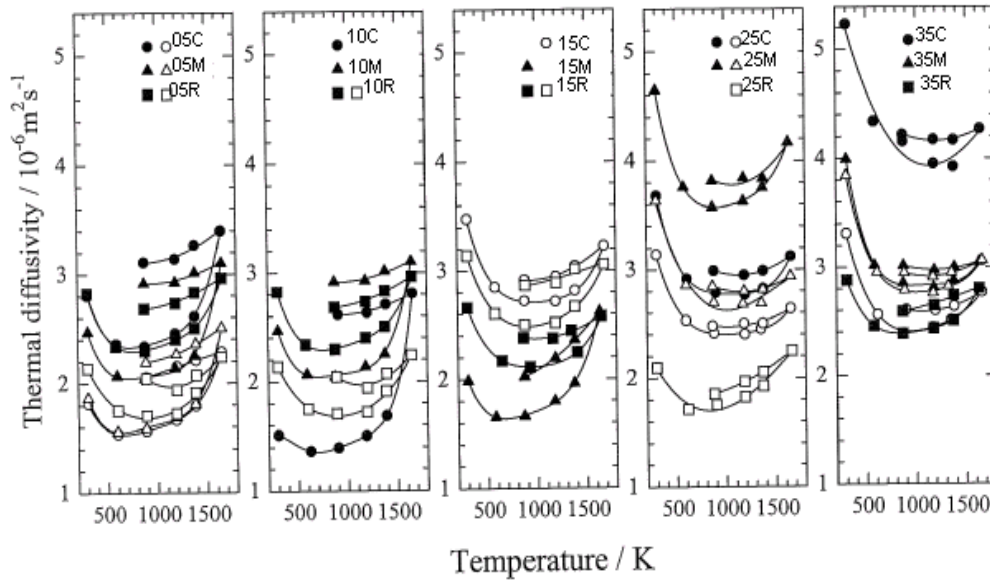


**Figure 37.** Temperature dependence of the apparent thermal diffusivities for coke samples taken from the levels 05-35.

It can be seen that the apparent thermal diffusivity decreases and starts to increase about 773 K with increasing temperature during heating cycle. During the cooling cycle, the apparent thermal diffusivity constantly decreases with decreasing temperature until 873 K. The increase and decrease in the thermal diffusivity during the respective heating and cooling cycles are considered to be due to the radiation effect. It can be also found that the apparent thermal diffusivity observed during the cooling cycle is larger than that observed during the heating cycle. The difference may be due to the graphitisation of the sample during the high temperature measurements.

**Figure 38** shows that the coke samples taken from deeper level of the blast furnace show larger graphitisation degree. It can be due to the thermal history of the coke samples.

**Figure 39** shows that the thermal diffusivity increases with increasing the value of  $L_c$ , i.e. the degree of graphitisation. This result may indicate that the thermal diffusivity of coke sample depends on the degree of graphitisation.

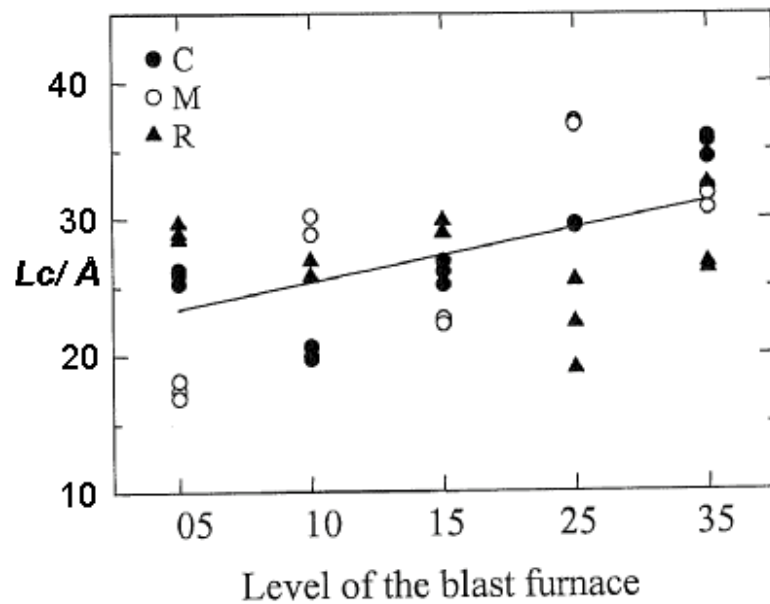


**Figure 38.** Values of  $L_c$  versus level of the blast furnace.

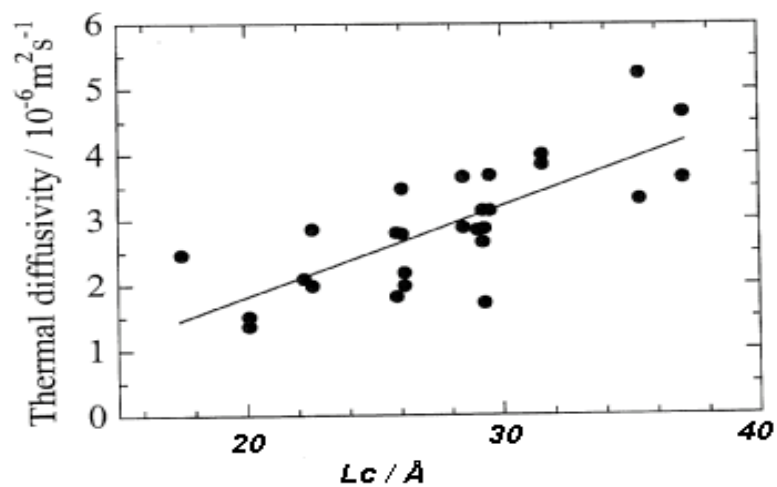


**Figure 39.** Thermal diffusivity at room temperature versus the average crystallite size along the structural c-axis,  $L_c$ .

### 3.5 General discussion

The thermal transport can be carried out by electrons as well as phonons depending on the type of the material. In the metallic alloys, which are good electric conductors, the thermal transport can mostly be carried out by electrons. On the other hand the contribution of the phonons, which refer to the lattice thermal conduction, can not be ignored. The comparison between the calculated thermal conductivity based on the electrical resistivity of the alloys and the measured values can be a good indicator to the electronic contribution of the heat conduction. The present study shows that the electron contribution depends on metal type, additional alloying elements, distribution of the non metallic inclusion and the inter-metallic phases in the structure.

The thermal conductivity is infinite if the carrier (phonon or electron) mean free path  $l$  is not limited by collision between themselves or between the carrier and lattice defects. Energy and momentum are conserved in a collision event, but because the carriers are mass-less particles, they may be annihilated or created [44]. As mentioned in equation (21), the phonon mean free path  $l$  is limited by collision with other carriers and with lattice defects. At high temperatures, the thermal conductivity must involve three or more phonons and electrons. It could be divided into two phenomena; a) when two carriers combine in a 'collision' event, and form one new phonon as shown in **Figure 40, a**. In this case 'n' in equation (2) will be proportional to  $T$  as it shown in linear part in **Figure 8, 13** and **16** of CMSX-4, 90Ti.6Al.4V and stainless steel alloys respectively b) when one phonon is annihilated to form two new phonons, **Figure 40,b**. In this case  $l$  is proportional to  $1/T$  as denoted in **Figures 29** and **37** of the mould flux and coke respectively

There may also be four phonons process as shown **Figures 40 c** and **40 d**. In this case  $l$  can be proportional to  $T^2$  or  $1/T^2$  respectively. At high temperature the disordering is increased, which decreases the mean free path as well as thermal diffusivity as shown in the second part of **Figures 8** and **13**.

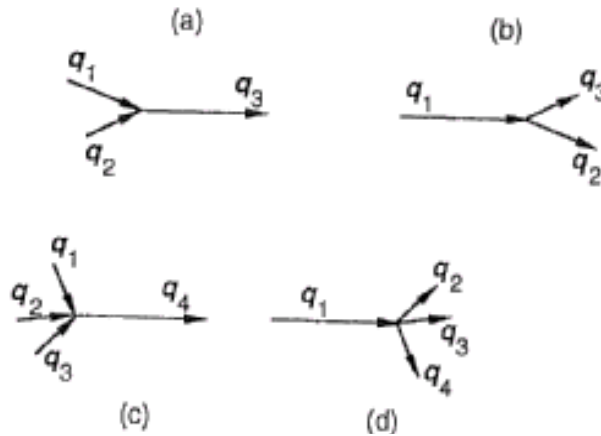


**Figure 40.** Three phonon (a,b) and four-phonon (c,d) scattering processes [44].

Analogously, the thermal diffusivity is increased with increasing the structure ordering i.e. crystallisation degree by increase annealing time as well as annealing temperature of mould flux **Figures 29, 30 and 39**. This increase could be due to reducing of point defects and crystal boundaries.

In liquid state, the disordering will be very high because of collision increasing between phonons themselves and phonon-electron. In this case the mean free path will be shorter than the characteristic distance between two neighboring atoms. At that time, the thermal diffusivity will be independent of temperature as shown in liquid CMSX-4 and liquid mould flux **Figures 11 and 31** respectively.

On the other hand the crystallisation degree is dependant on the chemical composition of material and the heat treatment condition (time, temperature) as shown in coke and mould flux materials.



#### 4. CONCLUSION

Thermal diffusivity, XRD and heat capacity measurements have been carried out of some industrially important systems, *viz.* alloys, metallic matrix composites, mould flux and coke used in the blast furnace.

For the alloys, the thermal diffusivity increases with increase in temperature of CMSX-4 nickel base and 90Ti. 6Al. 4V alloys at temperature below 1253 and 1225 K respectively. Above these temperatures the dissolving of intermediate phases such as  $\text{Ni}_3\text{Al}$  in CMSX-4 alloy and  $\text{Ti}_3\text{Al}$  in 90Ti.6Al.4V alloy increases the disordering in the structure and as a result, decreases the thermal diffusivity of these alloys.

Liquid CMSX-4 does not show any change of thermal diffusivity with temperature. It could be due to the decrease of the mean free path below characteristic distance between two neighboring atoms.

For 25Cr:6Ni stainless steel, the thermal diffusivity is nearly constant up to about 700 K. Beyond that, there is an increase with temperature both during heating as well as cooling cycle. On the other hand, the slope of the curve increases above 950 K, which could be due to the increase of bcc phase in the structure.

0.7% carbon steel shows a decrease in the thermal diffusivity at temperature below Curie point, where the structure contains bcc+ fcc phase. Above this point, the thermal diffusivity increases, where the structure contains only fcc phase.

The experimental thermal conductivity values of these alloys show good agreement with the calculated values using Mills model.

Thermal diffusivity measurements as a function of temperature on sintered AISI 304 stainless steel-alumina composites having various composition, *viz.* 0.001, 0.01, 0.1, 1, 2, 3, 5, 7, 8 and 10 wt%  $\text{Al}_2\text{O}_3$  were carried out in the present work.

The thermal diffusivity as well as the thermal conductivity were found to increase with temperature for all composite specimens. The thermal diffusivity/conductivity decreases with increasing weight fraction of alumina in the composites. The experimental results are in good agreement with simple rule of mixture, Eucken equation and developed Ohm's law model at weight fractions of alumina below 5 wt%. Beyond this, the thermal diffusivity/ conductivity exhibit a high discrepancy probably due to the agglomeration of alumina particles during cold pressing and sintering.

The thermal diffusivities of mould powder having glassy and crystalline state decrease with increase temperature at lower temperature and are constant at higher temperature except for one glassy sample.

The thermal diffusivity measurements of mould powder in liquid state do not show any significant change with temperature. It is considered that this is likely to be due to the silicate network being largely broken down. The thermal diffusivity is increased with increasing crystallisation degree of mould powder.

Thermal diffusivity measurements of coke samples taken from different level in the shaft of the blast furnace show that coke from deeper levels of the blast furnace exhibit larger thermal diffusivities. This is confirmed by XRD measurements showing an increase of the value of larger average crystallite size along the structural  $c$ -axis,  $L_c$  (which is indicative of the degree of graphitisation) with depth in the blast furnace. The coke sample having higher degree of graphitisation shows larger thermal diffusivity. The XRD and heat capacity measurements of coke samples show that the graphitisation of coke was instantaneous between 973 and 1473 K.

## **5. Future work**

1. Study the effect of the shape and the size of discontinuous phases on the thermal diffusivity of metallic matrix composites.
2. Study the effect of deformation percentage on the thermal conductivity of austenitic stainless steel.
3. Further investigation of the thermal conductivity of mould flux using in the steel production.





## REFERENCES

1. J. Ormerod, R.Tylor, J.Edward, *Metal Technology*, April, (1978).p.p 109-113.
2. K. C. Mills, A.P. Day, P.N.Quested, *Estimation the Thermophysical Laboratory*, Teddington, Middx.
3. R.A.Crane and R.I.Vachon, *Int.J.Heat Mass Transfer*, 2, 1969, pp. 249-264.
4. H. Shibata, T. Emi, Y. Waseda, K. Kondo, H. Ohta and K. Nakajima: *Tetsu-to- Hagane*, 82, (1996), pp. 504.
5. R. Taylor and K. C. Mills: *Ironmaking and Steelmaking*, 15, (1988), pp.187.
6. A.V. Oelreich, M.Sc. Thesis, Royal Inst.of tech.,Div.Mat.Proc.Sci.,(2004), ISRN KTH/MSE--04/20--SE+ THMETU/EX.
7. M. Kawakami, T.Karato, H.Tagu, T.Takenaka, S.Yokoyama ,*Science and Technology of Innovative Ironmaking for aiming at Energy Half Consumption*, November 27 to 28, 2003, Tokyo, Japan, pp. 49-53.
8. M. Hayashi, S. Gupta, T. Miyamoto, R. Abdul Abas, and S. Seetharaman, 'Thermal diffusivity of cokes taken from a pilot blast furnace', MSE, KTH; Stockholm, Sweden, unpublished research, (2003).
9. M.Hayashi, P.Fredriksson, S.Seetharaman, *Science and Technology of Innovative Ironmaking for aiming at Energy Half Consumption*, November 27 to 28, 2003, Tokyo, Japan, pp. 141-149.
10. R. E. Taylor, *High Temperature-High Pressure*, 11, (1979), pp.43-58.
11. J.T.Schirempf. *High Temp-High pressure*, 4, (1972), pp. 411-416.
12. W. J. Parker, R. J. Jenkins, C. P. Butler and G. L. Abbott: *J. Appl. Phys.*, 32, (1961), pp.1679.
13. Patrik Fredriksson, Doctoral Thesis, Royal Inst.of tech.,Div.Mat.Proc.Sci.,(2003), 3, ISRN KTH/MSE--03/36--SE+ THMETU/AVH.
14. H.P.Klug, L.E.Alexander, *X-ray diffraction procedures*, John Wiley & Sons, Inc., USA, 2:nd Ed., (1974). pp. 700-702.
15. NETZSCH Instruments, *Thermal analysis software , Proteus*, for MS Windows, ver 4.2, Aldridge, Weast Midlands UK, (2003).
16. Y. Tonooka, R. E. Aune and S. Seetharaman, unpublished work, Division of Materials Process Science, Royal Institute of Technology, Stockholm, Sweden, 2005.
17. P Quested, *National Physical Laboratory*, Teddington, Middx., UK
18. P. Debye: *Vorträge über die kinetische Theorie der Materie und Elektrizität*, Gottinger Wolfskehlvortrage. B. G. Teubner, Leipzig and Berlin, (1914), pp. 46.
19. M. Hayashi and S. Seetharaman, *ISS Transactions*, 2005.
20. G. Grimvall, "Thermophysical Properties of Materials", Publ. Elsevier Science B.V., Amsterdam, 1999.
21. K. C. Mills, Y. M. Youssef and Z. Li, Department of Materials, Imperial College London, Exhibition Road. London SW7, prepared for ISIJ .

22. K. C. Mills, NPL, Recommended values of thermophysical properties for selected commercial alloys, ASM International ISBN 0-87170-753-5, (2002), pp.25.
23. Y.Takahashi, International Journal of Thermophysics, 5, No.1, (1984), pp. 41-51.
24. R.J. Westover, R.W. Source: Journal of Chemical and Engineering Data, 7, No 3, July, (1962), pp. 434-437.
25. Y. S. Touloukian, R. W. Powell, C.Y. Ho and M. C. Nicolaou: Thermophysical Properties of Matter., 10, IF/PLENUM. New York, (1973), pp. 82.
26. A. Rudajevova and J. Burianek, Journal of Phase Equilibria , 22, No. 5, (2001), pp. 560-563.
27. G.D. Cody, B. Abeles, D.S. Beers: Metallurgical Society of American Institute of Mining, Metallurgical and Petroleum Engineering--Transactions, 221, No1, (1961), pp. 25-27.
28. <http://www.matweb.com/search/SpecificMaterial.asp>
29. JANAF Thermophysical Tables, Third Edition, 14, Supplement No.1, (1985).
30. R. W. Westover, R. J. Jenkins, Journal of Chemical and Engineering Data, 7, No 3, July, (1962), pp. 434-437.
31. B. W. James, G. H. Wostenholm, G. S. Keen, S. D. McIvor, J.Phys, D:Appl.Phys. 20, (1987), pp. 261-268.
32. K. Hayashi, T.M. Kyaw, Y. Okamoto, High Temperature-High Pressure, 30, (1998), pp.283-290.
33. M. Hayashi, R. Rajter, R. Morales, S. Seetharaman, Z.Metallkunde,94, 11, (2003), pp.1179-1184.
34. H. Shibata, T. Emi, Y. Waseda, K. Kondo, H. Ohta and K. Nakajima: *Tetsu-to- Hagane*, 82, (1996), pp. 504.
35. W. D. Kingery, H. K. Bowen and D. R. Uhlmann: Introduction to Ceramics, John Wiley & Sons, Inc., New York, (1976), pp. 612.
36. B. O. Mysen, D. Virgo and C. M. Scarfe: *Am. Mineralogist*, 65, (1980), pp. 690.
37. K. C. Mills: Slag Atlas, 2nd. ed., ed. by Verein Deutscher Eisenhüttenleute, Verlag Stahleisen GmbH, (1995), pp. 6.
38. M. Hayashi, T. Watanabe, K. Nagata and S. Hayashi: Tokyo Institute of Technology, unpublished research, (2002).
39. M. Hayashi, N. Nabeshima, H. Fukuyama and K. Nagata: *ISIJ International* 42, (2002), pp. 352.
40. R. Eriksson, M. Hayashi and S. Seetharaman: *Inter. J. Thermophys.*, 24 (2003), pp. 785.
41. N. A. Lapina, V. S. Ostrovski, K. I. Syskov, Carbon, 14, (1976), pp. 39-41.
42. T. Hossain, J. Pooder, Indian J. Phys, 72A (3), (1998), pp. 225-232.
43. E. Fitzner, S. Weisenburger, Carbon, 14, (1976), pp. 323-327.
44. G. Grimvall, "Thermophysical Properties of Materials", Publ. Elsevier Science B.V., Amsterdam, 1999.